

Air Force Institute of Technology

AFIT Scholar

Theses and Dissertations

Student Graduate Works

Fall 2019

Nonlinear Characterizing of a New Titanium Nitride on Aluminum Oxide Metalens

Michael A. Cumming

Follow this and additional works at: <https://scholar.afit.edu/etd>



Part of the [Optics Commons](#), [Plasma and Beam Physics Commons](#), and the [Semiconductor and Optical Materials Commons](#)

Recommended Citation

Cumming, Michael A., "Nonlinear Characterizing of a New Titanium Nitride on Aluminum Oxide Metalens" (2019). *Theses and Dissertations*. 3168.
<https://scholar.afit.edu/etd/3168>

This Thesis is brought to you for free and open access by the Student Graduate Works at AFIT Scholar. It has been accepted for inclusion in Theses and Dissertations by an authorized administrator of AFIT Scholar. For more information, please contact richard.mansfield@afit.edu.



**Nonlinear Characterizing of a New Titanium
Nitride on Aluminum Oxide Metalens**

THESIS

Michael Adam Cumming, 1 Lt, USAF
AFIT-ENP-MS-19-D-012

**DEPARTMENT OF THE AIR FORCE
AIR UNIVERSITY**

AIR FORCE INSTITUTE OF TECHNOLOGY

Wright-Patterson Air Force Base, Ohio

DISTRIBUTION STATEMENT A
APPROVED FOR PUBLIC RELEASE; DISTRIBUTION UNLIMITED.

The views expressed in this document are those of the author and do not reflect the official policy or position of the United States Air Force, the United States Department of Defense or the United States Government. This material is declared a work of the U.S. Government and is not subject to copyright protection in the United States.

AFIT-ENP-MS-19-D-012

NONLINEAR CHARACTERIZING OF A NEW TITANIUM NITRIDE ON
ALUMINUM OXIDE METALENS

THESIS

Presented to the Faculty
Department of Engineering Physics
Graduate School of Engineering and Management
Air Force Institute of Technology
Air University
Air Education and Training Command
in Partial Fulfillment of the Requirements for the
Degree of Master of Science in Physics

Michael Adam Cumming, B.S.P,B.S.M

1 Lt, USAF

29 August 2019

DISTRIBUTION STATEMENT A
APPROVED FOR PUBLIC RELEASE; DISTRIBUTION UNLIMITED.

AFIT/ENP/MS/19-D/012

NONLINEAR CHARACTERIZING OF A NEW TITANIUM NITRIDE ON
ALUMINUM OXIDE METALENS

THESIS

Michael Adam Cumming, B.S.P,B.S.M
1 Lt, USAF

Committee Membership:

Dr. M. Ferdinandus, PhD
Chairman

Dr. M. Marciniak
Member

Lt Col S. D. Butler, PhD
Member

Abstract

A sample metalens generated from Titanium Nitride deposited onto Aluminum Oxide was designed to focus at 10 microns with a beam centered at 800nm, and when analyzed with high intensity illumination was found to have a focal length of $9.650 \pm 0.003 \mu m$ at an intensity of $16.93 [MW/cm^2]$. Analyzing this change by comparing it to a Fresnel Lens' physics shows that for this lens, the effective nonlinear index of refraction is certainly greater than the nonlinear index of just Titanium Nitride itself, at $-1.6239 \times 10^{-15} [m^2/W]$ compared to the materials $-1.3 \times 10^{-15} [m^2/W]$. Analyzing this lens by taking it a step further and comparing it to a Fresnel Phase Zone Plate give a nonlinear index of 1.653×10^{-11} , which deviates from the materials nonlinear index even further, by over 4 orders of magnitude. This shows that the microscopic patterning of TiN in the correct geometric manner increases its effective nonlinear index by at least 4 orders of magnitude, but likely more.

Table of Contents

	Page
Abstract	iv
List of Figures	vii
I. Introduction	1
1.1 Background	1
1.2 Motivation	1
1.3 Problem	2
1.4 Hypothesis	2
1.5 Methods	3
1.6 Research Contributions	4
1.7 Outline	4
II. Theory	6
2.1 Optics Review	6
2.2 Linear Optics	8
2.3 Refractive Optics	10
2.4 Refractive Lenses	11
Fresnel Lenses	12
2.5 Diffractive Optics and Diffractive Lenses	14
Diffractive Fresnel Lens	15
Fresnel Zone Plates	16
Phase Reversal Zone Plates	17
Metasurfaces	19
Metalenses	19
Types of Diffractive Lens Focii	21
Strehl Ratio	24
2.6 Nonlinear Optics	25
Third Order Nonlinear Effects	26
2.7 Properties of Related Materials	29
Bulk Properties	29
Meta-atoms Used: Plasmonic Resonators	30
2.8 Focal Length Analysis	31
Center of Focus	31
$D4\sigma$	32
Power in a Bucket Method	34
Focal Dispersion Fitting	35
Focal Separation	36
2.9 Focal Analysis	37
Airy Fit	37

	Page
Strehl Ratio Analysis	38
Power in Bucket at Focus	39
2.10 Index Analysis	39
Refractive Lens Analysis	39
Zone Plate Analysis	41
III. Design and Methodologies	43
3.1 Lens Design	43
3.2 Lab Setup	43
3.3 Data Acquisition	49
IV. Results and Analysis	50
4.1 Data and Graphs	50
4.2 Focal Shift Across Scans	51
$D4\sigma$	51
Power in a Bucket	58
4.3 Change in Focal Shape Across Scans	65
Strehl Ratio	65
R^2 Value of fit to Airy	67
Maximum Bucket Values	69
4.4 n_2 Analysis From Fourier Lens Model	72
n_{ml} and n_{mnl} analysis	73
4.5 n_2 Analysis From Phase Zone Plate Model	74
V. Conclusions	76
5.1 Summary	76
5.2 Benefits and Limitations	77
5.3 Recommendations for Future Work	78
Appendices	80
A. Small Errors in Focal Length	81
Bibliography	84

List of Figures

Figure		Page
1.	(a) Shows a standard spherical lens divided into slice with equal height. The solid lines represent the lines that determine the width of each zone, while the dashed lines represent the cutting up of the zone. (b) Represents all extra glass cut out, such that just the outermost glass that is cut out from the black lines and dashed lines is left. (c) Is simply the middle figure with the cut pieces held together by a thin piece of material. 13
2.	(a) Shows a standard spherical lens divided into zones with equal width. The solid lines represent the lines that determine the width of each zone, while the dashed lines represent the cutting up of the zone. (b) Represents all extra glass cut out, such that just the outermost glass that is cut out from the black lines and dashed lines is left. (c) Is simply the middle figure with the cut pieces held together by a thin piece of material. 13
3.	This illustrates the relationship between the required phase change along a flat optic in order to focus at a single spot a distance l_0 away, in terms of the total distance from any point along the optics, to the focal point, l 16
4.	(a) The dots represent the designed location of the metalens. Rings are matched to the metalens in order to generate a phase profile. (b) Due to the radial symmetry of the lens, a two dimensional representation of the lens is used. The depth of the phase is determined by preset depths of the metapillars as well as of the index of the pillars. (c) This shows a sample example of a x-z profile of the focusing behavior of the phase profile generated using Rayleigh Sommerfield propagation. In this case, the x axis is arbitrary, and the scan is from 1 micron past the focus, to 15 microns 20

Figure	Page
5.	The left figure illustrates a flat lens with a very dense distribution of meta-atoms as well as many unique phase changes. The right figure illustrates the same as the left, but with fewer unique phase changes, leading to instead the black lines representing the effective wave front, and not all focusing perfectly. The black line is representative of the jagged wavefront resulting in fewer unique phase changes. The fewer unique phase changes, the more aberration is added to the wave front. 20
6.	The left figure illustrates the focusing of a spherical lens to a spot. The right image illustrates that because a meta-lens focuses to a point, it can be treated as a bulk spherical lens with an effective index of refraction. 21
7.	A Gaussian is superimposed above an Airy disk pattern with equal peak intensities. The x-axis represents the radial distance from the center of the distribution in terms of $\lambda \times$ f-number. Although the Gaussian is not normalized, the purpose is to illustrate the closeness of the curves to add justification that a Gaussian curve may be fit to a data set as an approximation when the data set is represented by an Airy Pattern. 22
8.	This figure is used to illustrate why the first moment of each slice is set to the location of the maximum intensity rather than of the calculated moment, which is clearly off center. This is just one example taken at an arbitrary slice, however the effect is present across all slices. 32
9.	(a)The thin straight lines represent the collimated beam moving towards the diffractive optic. The thicker solid lines on the other end of the diffractive optic represent the effective resulting wave front after diffraction, leading to the observer (in this case, the microscope objective) (b) Similar to (a), when the observer is closer to the lens, they see effectively diverging waves that, if traced backwards, would lead to a focus equal to one focal length of the lens behind the lens. The dashed thick red lines represent the virtual wavefront from behind the lens. 36

Figure	Page
10. Red dots represent the TiN deposits. This Figure shows the pattern of the TiN lens that we are analyzing. This is the design of the desired sample rather than what is actually manufactured.	43
11. The copper colored dots represent the actual Titanium Nitride deposited onto the Alumina substrate. All of these together combine to make the metalens being analyzed. The lens is 10 microns wide and long.	45
12. A basic diagram for the autocorrelator used to determine the pulse width. The beam enters from the bottom of the diagram and is incident to a beam splitter. One path of the beam hits a retroreflector and shines straight through to the detector. The other beam is incident on a retroreflector inside a delay drive that rapidly increases and decreases the beam path. The reflection rejoins the other path and is autocorrelated with it on a detector.	45
13. This figure illustrates the path of the beam as it progressing from the Griffin Oscillator to the sample, and through it to the microscope	48
14. (a) The blue figure at the top represents our microscope objective, the orange triangle represents where the objective is focusing, and the red pillar represents the laser light coming in from below. In this figure, the microscope is viewing strictly the sample. (b) The red triangle represents the virtual diverging virtual rays that cause the effect of viewing a focus behind the lens. (c) In this figure, the objective is viewing the rays that create the primary positive diffractive focus.	48

15. Illustrated is the $d=4$ Sigma values obtained when scanning near the focii for the sample illuminated with a beam of bandwidth centered at 800nm with a 25nm FWHM. After progressing through a neutral density filter, the power of the beam is 27.16mW, and the intensity at the sample is approximately $0.6761\text{MW}/\text{cm}^2$. Using the methods discussed in the Subsection “ $D4\sigma$ ” in Section 2.7, an array of $D4\sigma$ values are obtained for varying voltage readouts of the z-piezo motor near the focus of the sample. The results near the positive diffractive focus of the metalens are on the top, with the negative diffractive focus results being on the bottom. The minimum of the fitted curve is given by the dashed line. 52
16. Illustrated is the $d=4$ Sigma values obtained when scanning near the focii for the sample illuminated with a beam of bandwidth centered at 800nm with a 25nm FWHM. After progressing through a neutral density filter, the power of the beam is 27.16mW, and the intensity at the sample is approximately $0.6761\text{MW}/\text{cm}^2$. Using the methods discussed in the Subsection “ $D4\sigma$ ” in Section 2.7, an array of $D4\sigma$ values are obtained for varying voltage readouts of the z-piezo motor near the focus of the sample. The results near the positive diffractive focus of the metalens are on the top, with the negative diffractive focus results being on the bottom. The minimum of the fitted curve is given by the dashed line. 53
17. Illustrated is the $d=4$ Sigma values obtained when scanning near the focii for the sample illuminated with a beam of bandwidth centered at 800nm with a 25nm FWHM. After progressing through a neutral density filter, the power of the beam is 187.1mW, and the intensity at the sample is approximately $4.658\text{MW}/\text{cm}^2$. Using the methods discussed in the Subsection “ $D4\sigma$ ” in Section 2.7, an array of $D4\sigma$ values are obtained for varying voltage readouts of the z-piezo motor near the focus of the sample. The results near the positive diffractive focus of the metalens are on the top, with the negative diffractive focus results being on the bottom. The minimum of the fitted curve is given by the dashed line. 54

18. Illustrated is the $d=4$ Sigma values obtained when scanning near the focii for the sample illuminated with a beam of bandwidth centered at 800nm with a 25nm FWHM. After progressing through a neutral density filter, the power of the beam is 679.8mW, and the intensity at the sample is approximately 16.93MW/cm². Using the methods discussed in the Subsection “ $D4\sigma$ ” in Section 2.7, an array of $D4\sigma$ values are obtained for varying voltage readouts of the z-piezo motor near the focus of the sample. The results near the positive diffractive focus of the metalens are on the top, with the negative diffractive focus results being on the bottom. The minimum of the fitted curve is given by the dashed line. 55
19. Illustrated is the $d=4$ Sigma values obtained when scanning near the focii for the sample illuminated with a beam of bandwidth centered at 760nm with a 25nm FWHM. After progressing through a neutral density filter, the power of the beam is 32.863mW, and the intensity at the sample is approximately 0.818MW/cm². Using the methods discussed in the Subsection “ $D4\sigma$ ” in Section 2.7, an array of $D4\sigma$ values are obtained for varying voltage readouts of the z-piezo motor near the focus of the sample. The results near the positive diffractive focus of the metalens are on the top, with the negative diffractive focus results being on the bottom. The minimum of the fitted curve is given by the dashed line. 56
20. Illustrated is the $d=4$ Sigma values obtained when scanning near the focii for the sample illuminated with a beam of bandwidth centered at 840nm with a 25nm FWHM. After progressing through a neutral density filter, the power of the beam is 21.67mW, and the intensity at the sample is approximately 0.540MW/cm². Using the methods discussed in the Subsection “ $D4\sigma$ ” in Section 2.7, an array of $D4\sigma$ values are obtained for varying voltage readouts of the z-piezo motor near the focus of the sample. The results near the positive diffractive focus of the metalens are on the top, with the negative diffractive focus results being on the bottom. The minimum of the fitted curve is given by the dashed line. 57

21. Illustrated is the Power in a Bucket values obtained when scanning near the focii for the sample illuminated with a beam of bandwidth centered at 800nm with a 25nm FWHM. After progressing through a neutral density filter, the power of the beam is 27.16mW, and the intensity at the sample is approximately $0.6761\text{MW}/\text{cm}^2$. Using the methods discussed in the Subsection "Power in a Bucket Method" in Section 2.7, an array of Power in a Bucket Method values are obtained for varying voltage readouts of the z-piezo motor near the focus of the sample. The results near the positive diffractive focus of the metalens are on the top, with the negative diffractive focus results being on the bottom. The maximum of the fitted curve is given by the dashed line. 59
22. Illustrated is the Power in a Bucket values obtained when scanning near the focii for the sample illuminated with a beam of bandwidth centered at 800nm with a 25nm FWHM. After progressing through a neutral density filter, the power of the beam is 27.16mW, and the intensity at the sample is approximately $0.6761\text{MW}/\text{cm}^2$. Using the methods discussed in the Subsection "Power in a Bucket Method" in Section 2.7, an array of power values are obtained for varying voltage readouts of the z-piezo motor near the focus of the sample. The results near the positive diffractive focus of the metalens are on the top, with the negative diffractive focus results being on the bottom. The maximum of the fitted curve is given by the dashed line. 60

23. Illustrated is the Power in a Bucket values obtained when scanning near the focii for the sample illuminated with a beam of bandwidth centered at 800nm with a 25nm FWHM. After progressing through a neutral density filter, the power of the beam is 187.1mW, and the intensity at the sample is approximately 4.658MW/cm². Using the methods discussed in the Subsection “Power in a Bucket Method” in Section 2.7, an array of power values are obtained for varying voltage readouts of the z-piezo motor near the focus of the sample. The results near the positive diffractive focus of the metalens are on the top, with the negative diffractive focus results being on the bottom. The maximum of the fitted curve is given by the dashed line. 61
24. Illustrated is the Power in a Bucket values obtained when scanning near the focii for the sample illuminated with a beam of bandwidth centered at 800nm with a 25nm FWHM. After progressing through a neutral density filter, the power of the beam is 679.8mW, and the intensity at the sample is approximately 16.93MW/cm². Using the methods discussed in the Subsection “Power in a Bucket Method” in Section 2.7, an array of power values are obtained for varying voltage readouts of the z-piezo motor near the focus of the sample. The results near the positive diffractive focus of the metalens are on the top, with the negative diffractive focus results being on the bottom. The maximum of the fitted curve is given by the dashed line. 62
25. Illustrated is the Power in a Bucket values obtained when scanning near the focii for the sample illuminated with a beam of bandwidth centered at 760nm with a 25nm FWHM. After progressing through a neutral density filter, the power of the beam is 32.863mW, and the intensity at the sample is approximately 0.818MW/cm². Using the methods discussed in the Subsection “Power in a Bucket” in Section 2.7, an array of power values are obtained for varying voltage readouts of the z-piezo motor near the focus of the sample. The results near the positive diffractive focus of the metalens are on the top, with the negative diffractive focus results being on the bottom. The maximum of the fitted curve is given by the dashed line. 63

Figure	Page
26.	Illustrated is the Power in a Bucket values obtained when scanning near the focii for the sample illuminated with a beam of bandwidth centered at 840nm with a 25nm FWHM. After progressing though a neutral density filter, the power of the beam is 21.67mW, and the intensity at the sample is approximately 0.540MW/cm ² . Using the methods discussed in the Subsection “Power in a Bucket Method” in Section 2.7, an array of power values are obtained for varying voltage readouts of the z-piezo motor near the focus of the sample. The results near the positive diffractive focus of the metalens are on the top, with the negative diffractive focus results being on the bottom. The maximum of the fitted curve is given by the dashed line. 64
27.	Each red bar represents the Strehl Ratio for the positive diffractive focus, at the beam parameters described below the individual bars. The blue bars, conversely, represent the Strehl Ratio for the negative diffractive focii 66
28.	The surface in this 3D plot represents the Airy fit applied to the data points, whereas the dots are the data points. This sample is taken around the positive diffractive focus of the medium power scan (4.65MW/cm ²) with a bandwidth centered at 800 nm. Although it is not a perfect fit, and towards the outer rings it deviates more, it illustrates that the general shape of the focus is similar to an Airy. 67
29.	Each red bar represents the R^2 values for the positive diffractive focus when fit to an Airy Pattern, at the beam parameters described below the individual bars. The blue bars, conversely, represent the R^2 for the negative diffractive focii 68
30.	Each red bar represents the percent of positive diffractive focal power is at the positive diffractive focus. All red values then will clearly be 1 then, they are included for better visual comparison to their negative diffractive focus values. The blue bars, conversely, represent the percent of positive diffractive focal power is at the negative diffractive focus 70

Figure	Page
31. A second order Fourier Curve is fit to the data points, with an x_0 offset. There is a very large uncertainty in the x_0 , but the other values have relatively low uncertainties.	81
32. Without any " x_0 ", Matlab provides its automated second order Fourier fit and the outputs for the individual variables can be seen, all with reasonable uncertainty.	82
33. Similar to the base Fourier fit with " x_0 " included, however the results from Matlabs' Fourier fit are plugged into the variables, leaving only the x_0 to be solved for.	83

NONLINEAR CHARACTERIZING OF A NEW TITANIUM NITRIDE ON ALUMINUM OXIDE METALENS

I. Introduction

1.1 Background

Metalenses and metasurfaces are a type of diffractive optic that controls light on the subwavelength scale. These surfaces are generated by depositing small resonating structures in such a geometry as to create a phase profile. These incredibly small structures have limited broadband steering and control, and one of the interests in them is determining how they react to various wavelengths. [1] Currently, much of this field of research has been focused around gold and silver, which have low thermal resistances and are not nearly as hard as Titanium Nitride [2] making them non-ideal candidates for studying third-order non-linear effects in metalenses, and limiting their potential applications due to them being more delicate. Using Titanium Nitride in metalenses is gaining popularity, in part due to its capability of overcoming those problems. TiN also is highly thermally conductive, thus allowing for high nonlinear effects when irradiated by high intensity beams. [3]

1.2 Motivation

Although there are many studies analyzing metalenses in the linear regime, the realm of nonlinear metasurface research remains fairly uncharted. Titanium Nitride is used in metasurfaces for single phase elements and arrays of those elements, and

for reasons discussed above as well as reasons to be discussed, this sample will be used in trying to understand how metalenses focus in non-linear regimes. [2]

1.3 Problem

Thus far, although a method for manufacturing meta lenses with Titanium Nitride exists, a detailed analysis of these lenses across high intensities have yet to be conducted. Determining the properties of these lenses when illuminated with various intensities and at multiple wavelengths is the next step to continuing research on the meta-lenses and vectoring what the next step in this field is, and how viable metalenses are in nonlinear focusing.

1.4 Hypothesis

Once analyzed at high enough intensities, the focal length of these samples should decrease relative to focal lengths observed at lower intensities. The tightening of the focus is partially due to Titanium Nitrides sizeable nonlinear susceptibility of $\chi^{(3)} = -5.3 \times 10^{-18}[m^2/V^2]$, which corresponds to a nonlinear index of $n_2 = -1.3 \times 10^{-15}[m^2/W]$ [4]. Due to the pattern of the meta-atom deposits on the metalenses, the resulting nonlinear indexes of refraction should be at least multiple times that of the bulk material used in the meta-atom deposits. If these lenses produce indexes of refraction significantly higher than those of the material itself, it will speak to the viability of using Titanium Nitride as a nonlinear metalens and as a candidate for optical computing as well as other applications. For optical computing, photons would need to be able to be steered and directed precisely over short distances, and being able to do that based solely on intensity would be a first big step towards the

realization of this application.

1.5 Methods

In analyzing these samples to determine their index at high intensities, a Griffin 5 oscillator is used and its' beam is focusing through a system of mirrors and two lenses, bringing the resulting beam down to a focal spot size of about 25 microns onto the microscope stage. The microscope stage has a fine three directional control piezo stage mount that the sample sits on, accurate to movements of $0.0309 \pm 0.0004 \mu m$, providing for precise manipulation of the sample relative to the microscope objective. Once the locations of the microlenses are determined on the sample slide with the microscope, small vertical adjustments are made with the piezo stage until the approximate locations of the focus of the lenses are found. A software tool is then used to record 1000 images of the phase for each of the planes the piezo scans relative to the sample, changing in steps of the mentioned 30.9 nm each time. Using Matlab[®] code, the data is processed and the most accurate location of the focuses of the samples across various intensities and wavelengths are obtained.

1.6 Research Contributions

Dr. Manuel Ferdinandus consistently helped brainstorm ideas for how to do the focal scans as well as provided me with the necessary equipment to do the scans.

Thaddeus Reese provided the samples as well as background on the lenses, and always available for questions and clarifications so that I could hone in to exactly what I was trying to find.

Dr Urbas Augustine provided help in understanding the use of the microscope, various other detection devices, and with getting the laser to sufficiently high power to be able to observe the nonlinear effects.

Dr Jamie J Gengler provided aid in brainstorming methods of getting the apparatus set up and general help with finding equipment to use in the lab.

Dr. Michael Marciniak and Lt. Col. Samuel Butler in helping me refine my analysis and lead me on paths that greatly improved my understanding of the material.

1.7 Outline

This thesis will begin by giving a review of the fundamental physics concepts that are present in this experiments. The review will move from the broad field of electrodynamics, to narrow down to the concepts behind both plasmonic meta-surfaces as well as non-linear focusing. After the physics of the relevant concepts is discussed, the assumptions that are used to tie this experiment to those concepts, as well as describing the experiment itself will be addressed.

The focusing of the metalens was found to have nonlinear focusing effects beyond

ones expected from the material they were made of alone. The results that lead to the final conclusion are given in various different ways. Different methods to analyze both the focal distance as well as the focal spot are applied to thoroughly analyze the behavior of the metalens used. After the behavior of the lens is discussed, the results of said discussion are used to solve for effective nonlinear refractive index values of the metalens if the metalens is treated as a fresnel lens.

II. Theory

This chapter covers the theory behind the experiment that is discussed in this document.

2.1 Optics Review

Optics is the study and application of how various materials affect the properties of incident or traveling electromagnetic waves. In 1873 James Maxwell developed his four equations that govern the properties of electromagnetic waves. In SI units, these general equations that represent travel through any medium are [5]

$$\nabla \cdot \mathbf{D} = \rho_f \quad (1)$$

$$\nabla \cdot \mathbf{B} = 0 \quad (2)$$

$$\nabla \times \mathbf{E} + \frac{\partial \mathbf{B}}{\partial t} = 0 \quad (3)$$

$$\nabla \times \mathbf{H} - \frac{\partial \mathbf{D}}{\partial t} = \mathbf{J}_f \quad (4)$$

where \mathbf{E} is the electric field, \mathbf{D} is the electric displacement field, \mathbf{B} is the magnetic field, \mathbf{H} is the magnetic field intensity, ρ_f is the free charge density, and \mathbf{J}_f is the free current density. \mathbf{D} and \mathbf{H} are defined as

$$\mathbf{D} = \epsilon_0 \mathbf{E} + \mathbf{P} \quad (5)$$

$$\mathbf{H} = \frac{1}{\mu_0} \mathbf{B} - \mathbf{M} \quad (6)$$

where ϵ_0 is the permittivity of free space, μ_0 is the permeability of free space, \mathbf{P} is the

polarization of the material the wave is traveling through, and \mathbf{M} is the magnetization of the material. Note, that Equation (5) and Equation (6) can be written in terms of \mathbf{E} and \mathbf{B} , such that

$$\mathbf{E} = \mathbf{D}/\epsilon_0 - \mathbf{P}/\epsilon_0 \quad (7)$$

$$\mathbf{B} = \mu_0\mathbf{H} + \mu_0\mathbf{M} \quad (8)$$

Equations (1), (2), (3) and (4) govern the physics of light in all situations. These equations are a set of coupled, first-order, partial differential equations. In uncoupling the following is applied:

$$\nabla \times \nabla \times \mathbf{V} = \nabla(\nabla \cdot \mathbf{V}) - \nabla^2\mathbf{V} \quad (9)$$

where \mathbf{V} is any vector field. Applying this equality to the curl of 3 and 4 yields:

$$\nabla \times \nabla \times \mathbf{E} = \nabla(\nabla \cdot \mathbf{E}) - \nabla^2\mathbf{E} = \frac{\partial}{\partial t}(\nabla \times \mathbf{B}) \quad (10)$$

$$\nabla \times \nabla \times \mathbf{H} = \nabla(\nabla \cdot \mathbf{H}) - \nabla^2\mathbf{H} = \frac{\partial}{\partial t}(\nabla \times \mathbf{D}) + \nabla \times (\mu_0\mathbf{J}_f) \quad (11)$$

In many cases, and certainly in the cases discussed in this paper, \mathbf{J}_f and ρ_f are both equal to zero as these materials are source free. From here, plugging in Equation (1) and Eqn. (2) into the middle equalities of Equation (10) and Equation (11) and applying the source free assumptions, Equation (10) and Equation (11) become,

$$-\frac{1}{\epsilon_0}\nabla(\nabla \cdot \mathbf{P}) - \nabla^2\mathbf{E} = \frac{\partial}{\partial t}(\nabla \times \mu_0\mathbf{M} + \mu_0(\epsilon_0\frac{\partial\mathbf{E}}{\partial t} + \frac{\partial\mathbf{P}}{\partial t})) \quad (12)$$

$$-\nabla(\nabla \cdot \mathbf{M}) - \nabla^2\mathbf{H} = \frac{\partial}{\partial t}(-\epsilon_0\mu_0(\frac{\partial\mathbf{H}}{\partial t} + \frac{\partial\mathbf{M}}{\partial t}) + \nabla \times \mathbf{P}). \quad (13)$$

Assuming $\nabla \cdot \mathbf{P} = 0$ and $\nabla \cdot \mathbf{M} = 0$, and as $1/c_0^2 = \mu_0\epsilon_0$ with c_0 being the speed of light in a vacuum, the above can be simplified down to,

$$\nabla^2\mathbf{E} + \frac{1}{c_0^2}\frac{\partial^2\mathbf{E}}{\partial t^2} = -\mu_0\frac{\partial}{\partial t}(\frac{\partial\mathbf{P}}{\partial t} + \nabla \times \mathbf{M}) \quad (14)$$

$$\nabla^2\mathbf{H} + \frac{1}{c_0^2}\frac{\partial^2\mathbf{H}}{\partial t^2} = -\frac{1}{c_0^2}\frac{\partial^2\mathbf{M}}{\partial t^2} + \nabla \times \mathbf{P}. \quad (15)$$

Applications of the above to various systems all lie in the manipulation of boundary conditions, and initial conditions when solving these equations. These form the basis for further in depth discussion of the applicable physics to the experiment addressed in this paper.

2.2 Linear Optics

Optics falls into one of two categories; linear optics, and nonlinear optics. If any medium is approximated as a collection of electric dipoles, then when the material is irradiated by an external oscillating electric field, they all will also oscillate and radiate. The term used to describe the collective radiation is the material's polarization or the polarization density, \mathbf{P} . Linear optics assume that the polarization density of the materials involved respond linearly to the incident electromagnetic fields, such that, [6]

$$\mathbf{P} = \epsilon_0 \chi \mathbf{E} \quad (16)$$

where χ is the electric susceptibility. Combining this with the relationship that,

$$\mathbf{M} = \chi_M \mathbf{H} \quad (17)$$

where χ_M is the magnetic susceptibility, it allows for a simplification to Equation (5) and Equation (6) such that

$$\mathbf{D} = \epsilon_0 \epsilon_r \mathbf{E} \quad (18)$$

$$\mathbf{H} = \frac{1}{\mu_0 \mu_r} \mathbf{B} \quad (19)$$

where

$$\epsilon_r = 1 + \chi \quad (20)$$

$$\mu_r = 1 + \chi_M. \quad (21)$$

Plugging these simplifications into Equation (9), allows Equation (14) to become,

$$\nabla^2 E = \mu_0 \mu_r \epsilon_0 \epsilon_r \frac{\partial^2 E}{\partial t^2} \quad (22)$$

This second order differential equation and its solutions form the basis for the field of linear optics. Although nonlinear optics, and effective non-linear coefficients play a role in the analysis to the lens in this thesis, before addressing the relevant nonlinear optics of the system, it is important to give an overview of refractive optics

and diffractive optics in the linear realm first.

2.3 Refractive Optics

Refraction is the change in direction of a wave when it passes from one medium to the next. Refractive optics then is changing of direction of electromagnetic waves when moving between mediums due to the properties of the mediums. In refractive optics, the electromagnetic radiation paths can be approximated using geometrical ray tracing, combined with the implementation of Snell's law. This approximation is called the eikonal approximation in optics and is valid as long as the size of the obstacle is large compared to the wavelength of light incident upon it. [7] For most lenses, it is furthermore assumed that the material is homogenous, rather than the lens being composed of numerous material's, allowing for the analysis to be simplified to changes strictly at the lens boundaries. The generalized Snell's Law, derived using Fermat's principle, states [8], [9]

$$n_t \sin(\theta_t) - n_i \sin(\theta_i) = \frac{\lambda_0}{2\pi} \frac{d\phi}{dx} \quad (23)$$

$$\sin(\theta_r) - \sin(\theta_i) = \frac{\lambda_0}{2\pi n_i} \frac{d\phi}{dx} \quad (24)$$

Where n_i, n_r , and n_t are the indexes of refraction for the incident, reflected, and transmitted rays respectively, θ_i, θ_r and θ_t are the incident, reflected, and transmitted angles, λ_0 is the wavelength of the incident light, and $\frac{d\phi}{dx}$ represents the change in phase discontinuities present at the boundary of a material with respect to an arbitrary x -direction in the plane of the sample.

In refractive optics, it is assumed that the right hand sides of Equation (23) and

Equation (24) are both zero, and this is what allows the paths of the beam to be governed by bulk properties of the materials involved. With little to no engineered phase discontinuities in refractive optics, much of the field of optics is governed by the manipulation of incident angle to boundaries, and the manipulation of constitutive parameters. [10]

2.4 Refractive Lenses

When the manipulation of constitutive parameters and angles of incident waves are engineered into an optical element in such a way to cause the transmitted (or reflected) rays to behave in a desired manner, instead of the broad term of 'optics' this behavior is narrowed down to beam steering. When the desired behavior is focusing the resulting waves, the material is further narrowed to talking about refractive lenses. In creating these lenses there are two equations, beyond Snell's Law, that represent most of refractive lenses, and certainly the lens comparisons that will be made in this thesis; the thin lens equation, and the lens' makers equation. The thin lens equation is given by:

$$\frac{1}{f} = \frac{1}{s_O} + \frac{1}{s_I} \quad (25)$$

where f is the focal length of the lens, s_O is the distance of the object from the lens, and s_I is the distance of the image formed by the lens, from the lens. This equation is used when the lens is thin enough that the propagation distance is small compared to the profile of the light hitting the lens and when the rays are close to the central axis of the lens.

The other equation is the lens maker's equation, given as,

$$\frac{1}{f} = \left(\frac{n_{lens}}{n_{adjacent}} - 1 \right) \left(\frac{1}{R} - \frac{1}{R'} \right) \quad (26)$$

where f is the focal length of the lens, n_{lens} is the refractive index of the material the lens is made of, n_s is the index of the material surrounding the lens, and R, R' are the radii of curvature on either side of the lens. [11]. Both of these equations are applications of Snell's law, however in these forms, it is easier to represent behavior when dealing with refractive lenses, as well as in understanding why non-spherical refractive lenses, such as Fresnel lenses are engineered the way they are.

Fresnel Lenses.

In 1822 French physicist Augustin Fresnel invented a lens that is today known as a Fresnel lens. The idea behind most larger scale Fresnel lenses is not dissimilar to more common spherical lenses. In refractive lenses, the path of light is determined by the angles at which the electromagnetic waves are incident on the boundaries, and the precise thickness of the material it travels through does not matter so long as thin lens equation approximation mentioned above is valid. As such, Fresnel took an ordinary lens, and in ring intervals, removed extra glass in the center, and just kept the boundary curvatures. There are two primary methods of determining the ring width when fabricating refractive Fresnel lenses. The first, is to keep the rings a constant width, and continue to expand them outwards. As towards the outside, relative to the direction of focusing the slope of the glass is steeper, the Fresnel lens ends up wider towards its outer edges.

The second method, and the one that is more closely related to the sample analyzed in this thesis, is having the rings vary in width, so long as each zone has a

constant maximum height from the edge of the lens. Both of these cases are illustrated in Figure 1 and Figure 2.

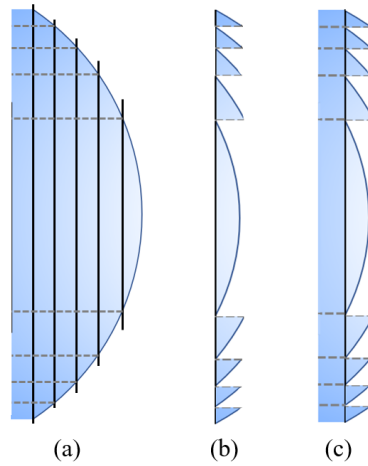


Figure 1. (a) Shows a standard spherical lens divided into slice with equal height. The solid lines represent the lines that determine the width of each zone, while the dashed lines represent the cutting up of the zone. (b) Represents all extra glass cut out, such that just the outermost glass that is cut out from the black lines and dashed lines is left. (c) Is simply the middle figure with the cut pieces held together by a thin piece of material.

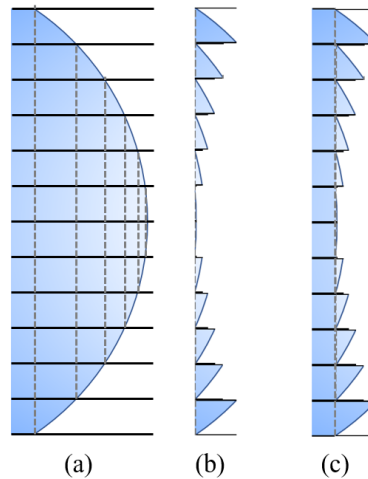


Figure 2. (a) Shows a standard spherical lens divided into zones with equal width. The solid lines represent the lines that determine the width of each zone, while the dashed lines represent the cutting up of the zone. (b) Represents all extra glass cut out, such that just the outermost glass that is cut out from the black lines and dashed lines is left. (c) Is simply the middle figure with the cut pieces held together by a thin piece of material.

2.5 Diffractive Optics and Diffractive Lenses

Wherever optics or light interactions with matter are present, diffraction is as well. In many cases, refractive effects are large enough that the diffractive contributions are negligible. As discussed, whereas refraction is the change in direction of a wave due to the bulk materials of a wave (such as index of refraction), diffractive optics is the manipulation of boundary conditions to change a wavefront. Just as with refraction, when this manipulation is for the purpose of changing the behavior of incoming light, it is called diffractive beam steering. Diffractive optics are appealing due to their capability to manipulate and control light using significantly less matter, having less mass, and taking up less space than their refractive counterparts. Furthermore, when the resultant beam behavior is to focus the incident waves, the optic is classified as a diffractive lens, and diffractive lenses are the area of interest in this thesis. In describing lenses, even in cases where refraction dominates, the resolution and the smallest spot size achievable are both diffraction limited by, at minimum, the diffraction that occurs at the aperture stop of the system (such as the edge of a lens; the object limiting the amount of light present at the image).

Although when dealing with diffraction, the generalized Snell's law is valid and still applies (as long as the phase gradient is not infinite along any points along the lens), analysis using in this manner can be rather complex. An alternate method of analysis that is easier is analyzing the wavefront using Huygen's principle. Huygen's principle states that every point along a wavefront can be treated as a secondary wavelet, or a source. The behavior of the electromagnetic wave can then be determined by superimposing the waves from all of the wavelets together. The principle of superposition allows addition of the phases of the waves generated by the effective sources together with one another to get a new resultant wavefront, which also can be broken down in the same manner. In the field of diffractive lenses, a few

designs dominate, and some of them are modified and taken from similar refractive designs. For this work, all of the diffractive lenses come from the same idea that is used in Fresnel lenses. Taking the idea of Fresnel lenses into the field of diffraction, the general physics for focusing using diffraction follows, which forms the basis for most metalenses. Most metalenses and Fresnel Zone Plates are applications of the idea of Fresnel lenses to diffraction lenses, but with some very important differences to be discussed. The lens analyzed here combines the both ideas.

Diffractive Fresnel Lens.

When discussing Fresnel lenses in refractive optics, one method of determining the zone size is by starting a new zone as soon as the material extends out to a predetermined distance. If this idea is taken to the regime where the lens is as flat as possible, diffraction begins to dominate. In this case, the lens can be approximated as flat and is analyzed using Huygen's principle. In order then for the lens to focus most efficiently (both tightest spot, and with the most constructive interference), there must be an introduced phase gradient across the lens, such that each wavelet's extra distance to the transverse focus is subtracted by a phase added or subtracted at the source location of that wavelet. The extra distance can be expressed as $l - l_0$, where l is the distance traveled, and l_0 is the axial distance to the focus. As such, the phase gradient needs to be equal to

$$\phi(l) = -k(l - l_0). \quad (27)$$

where ϕ represents the phase at any given point and k is the wavevector for the electromagnetic wave. This system is shown in Figure 3. Rewriting k and $l - l_0$, in terms of the wavelength of the light λ , the focal length f , and a distance along the

lens relative to the center, r , produces, [12]

$$\phi(r) = -\frac{2\pi n_{eff}(r)}{\lambda_0} d_{post}(\sqrt{f^2 + r^2} - f) = \frac{2\pi}{\lambda}(f^2 - \sqrt{f^2 + r^2}). \quad (28)$$

Although a Fresnel lens is not perfectly flat, the geometry of the ridges are designed so that the radial distances from the center imparts this phase change. In order to make the lens as thin as possible, with no phase delay, then every time r increases an extra λ distance, a new ridge will start so the phase delay is reset to zero. Figure 1 illustrates this in practice. All flat lens designed that will be mentioned are based off of this concept, off of Equation (28).

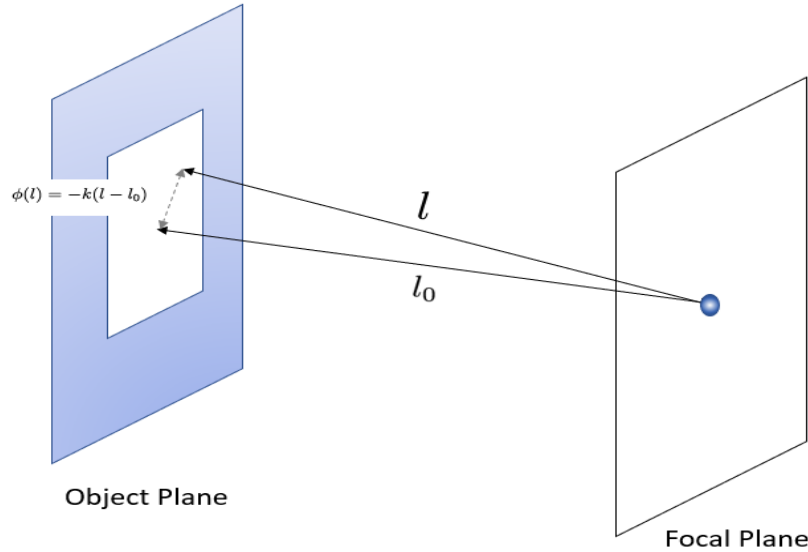


Figure 3. This illustrates the relationship between the required phase change along a flat optic in order to focus at a single spot a distance l_0 away, in terms of the total distance from any point along the optics, to the focal point, l

Fresnel Zone Plates.

Fresnel Zone Plates are the first, and technically only flat lens discussed in this section, however it is important to address the idea of Fresnel Zones, and the ideas

behind Fresnel Zone Plates, as they are applicable to metalenses as a whole, and the lens that will be analyzed in this thesis more specifically.

Consider Equation (28), however rather than imparting the phase change, the effects of the wavelets coming from the lens are analyzed at the focus. All wavelets within a $k/2$ distance from the center constructively interfere, however the next set of $k/2$ wavelets will destructively interfere (due to the nature of sine functions), while the following set will constructively interfere again, continuing on. The idea behind Fresnel Zone plates, is that each $k/2$ zone that constructively interferes is left as is. As for the zones that would normally destructively interfere, one of two things is normally done. The first is to just block out transmission from those zones completely. The other tactic is to instead coat those zones with phase-delaying material such that they impart a $k/2$ phase delay and instead of destructively interfering at the center, they constructively interfere at the center.

Phase Reversal Zone Plates.

Although the first zone plates created, were designed with the premise of simply blocking the light that would cause destructive interference, an alternate type of zone plate used today is known as a "phase zone plate" or "phase reversal zone plate." The zone plates operate in the same manner as the already discussed Fresnel zone plates, except rather than blocking the light that would cause destructive interference, a material is deposited onto that location of the plate that would cause a π phase delay, allowing that section to instead cause constructive interference at the focus again.

Comparing the metalens to a phase zone plate is one step closer to providing a more accurate representation of the lens. The pillars on the meta-lens are distributed

into rings, and by matching the outer radius of each ring and inner radius as the radii of the phase zone plate as shown in Figure 4, a phase profile is generated. That profile is then Rayleigh Sommerfeld propagated over a range of distances near the focus. This propagation first comes from Fourier transforming the phase profile;

$$U'(t) = \frac{1}{2\pi} \int_{-\infty}^{\infty} U(x) \exp i\omega x dx \quad (29)$$

Where $U'(t)$ is the profile in Fourier Space, $U(x)$ is the object profile, and omega and From here, the result is multiplied by the Rayleigh Sommerfeld kernel, and then inverse Fourier transformed to get back into position space. The is done many z distances and put together to obtain the mapping shown in Figure 4 C. The Rayleigh Sommerfeld Kernel is

$$\| = -\frac{i}{\lambda} \frac{1}{\sqrt{x^2 + z^2}} \exp ik\sqrt{x^2 + z^2}, \quad (30)$$

leading the inverse fourier transform which gives us the field distribution to be

$$U(x, z) = \frac{1}{2\pi} \int_{-\infty}^{\infty} U'(t) \| \exp -i\omega x d\omega \quad (31)$$

The phase delay comes from the index as well as the depth of the material, causing an effective increased distance that the light ha through as opposed to light passing through air. In this thesis, by setting the depth of the meta-lens pillars to the depth of the phase zone plate, the index is manipulated until the phase zone plate generates the largest amount of constructive interference at the observed focal lengths. This provides the effective index of the phase zone plate.

Metasurfaces.

Metasurfaces are created by depositing an array of subwavelength resonators commonly known as meta-atoms. The meta-atoms are much smaller than the wavelength of incident electromagnetic waves, so they do not meet the eikonal approximation for refractive optics, and are instead governed by diffractive effects. The bulk constitutive properties of metasurfaces (permittivity, permeability, and index) are not of much interest, however effective constitutive properties can be derived if the metasurface is treated as a bulk surface. [13] This treatment is key in the following sections.

Metalenses.

Metalenses utilize geometric shaping of sub wavelength rods and diffractive optics to focus incident light. [14] The geometry of the subwavelength rods, or the meta-atoms, is determined by (28). The height of the meta-atoms determines the phase change, however as will be discussed, for specific wavelengths, height manipulation requires manipulation of other properties of the meta-atom. [15] As different rods impart different phases changes, in creating metalenses and determining the pattern in which the rods can be placed, the first step is determining how many different heights of the meta-atoms (and hence how many unique abrupt phase changes) can be machined. For any material used, it is ideal to utilize the maximum number of unique phase changes possible [16]. Some materials prove to be more difficult to machine and manipulate at such small size scales than others. As such, the limiting factor in how many phase levels can be made often comes down to capabilities of manipulating the deposited material at those sizes. The effects of increasing (or decreasing) the number of unique phase changes, or number of different rods used, is illustrated in Figure 5. [16]

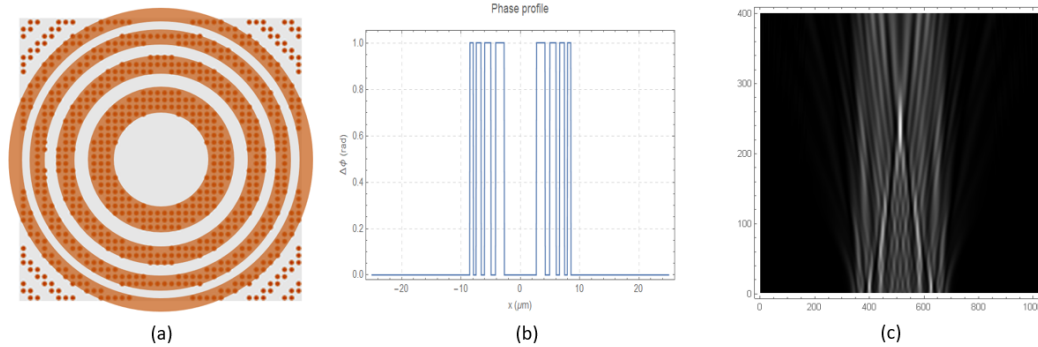


Figure 4. (a) The dots represent the designed location of the metalens. Rings are matched to the metalens in order to generate a phase profile. (b) Due to the radial symmetry of the lens, a two-dimensional representation of the lens is used. The depth of the phase is determined by preset depths of the metapillars as well as of the index of the pillars. (c) This shows a sample example of a x - z profile of the focusing behavior of the phase profile generated using Rayleigh Sommerfeld propagation. In this case, the x axis is arbitrary, and the scan is from 1 micron past the focus, to 15 microns

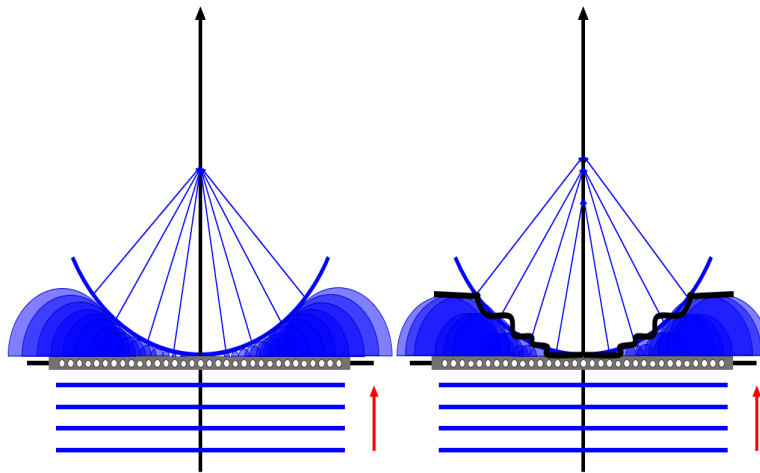


Figure 5. The left figure illustrates a flat lens with a very dense distribution of meta-atoms as well as many unique phase changes. The right figure illustrates the same as the left, but with fewer unique phase changes, leading to instead the black lines representing the effective wave front, and not all focusing perfectly. The black line is representative of the jagged wavefront resulting in fewer unique phase changes. The fewer unique phase changes, the more aberration is added to the wave front.

As these flat lenses have refractive lens properties, and are used as alternatives to traditional refractive lenses, it is important to be able to compare them to traditional lenses. Although metalenses are diffractive lenses, and diffraction describes the focusing behavior of the lens, when strictly analyzing the location of the focus, they can be modeled using geometric optics and where they focus can be analyzed as such. This modeling is shown in Figure. 6 and it allows us to solve for, and assign, effective constitutive parameters, namely, index of refraction. This modeling is strictly used to compare focusing performance to refractive optics and gain a better understanding of where the lens will focus as wavelength or intensity change. The varying methods of doing this will be discussed after a review of non-linear optics.

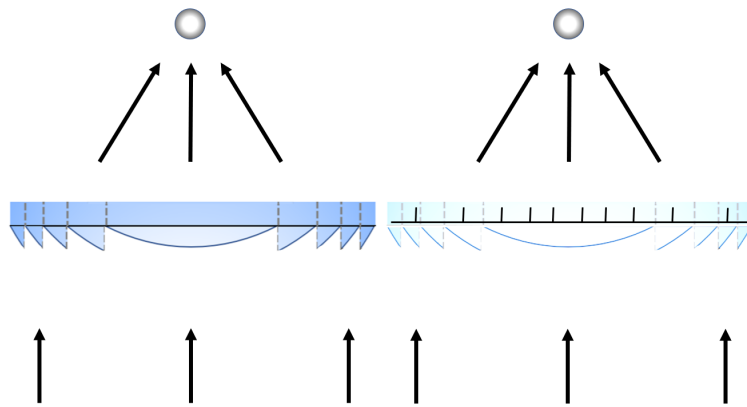


Figure 6. The left figure illustrates the focusing of a spherical lens to a spot. The right image illustrates that because a meta-lens focuses to a point, it can be treated as a bulk spherical lens with an effective index of refraction.

Types of Diffractive Lens Focii.

Although an Airy pattern approximation can be fit to the lenses transverse intensity distributions, and doing so yields two methods of determining where our focus is, Airy patterns' RMS spotsizes is undefined. Another function that is very similar to an Airy pattern, however has a very easily defined RMS is a Gaussian. Figure 7

illustrates a Gaussian profile superimposed above the central lobe of an Airy pattern.

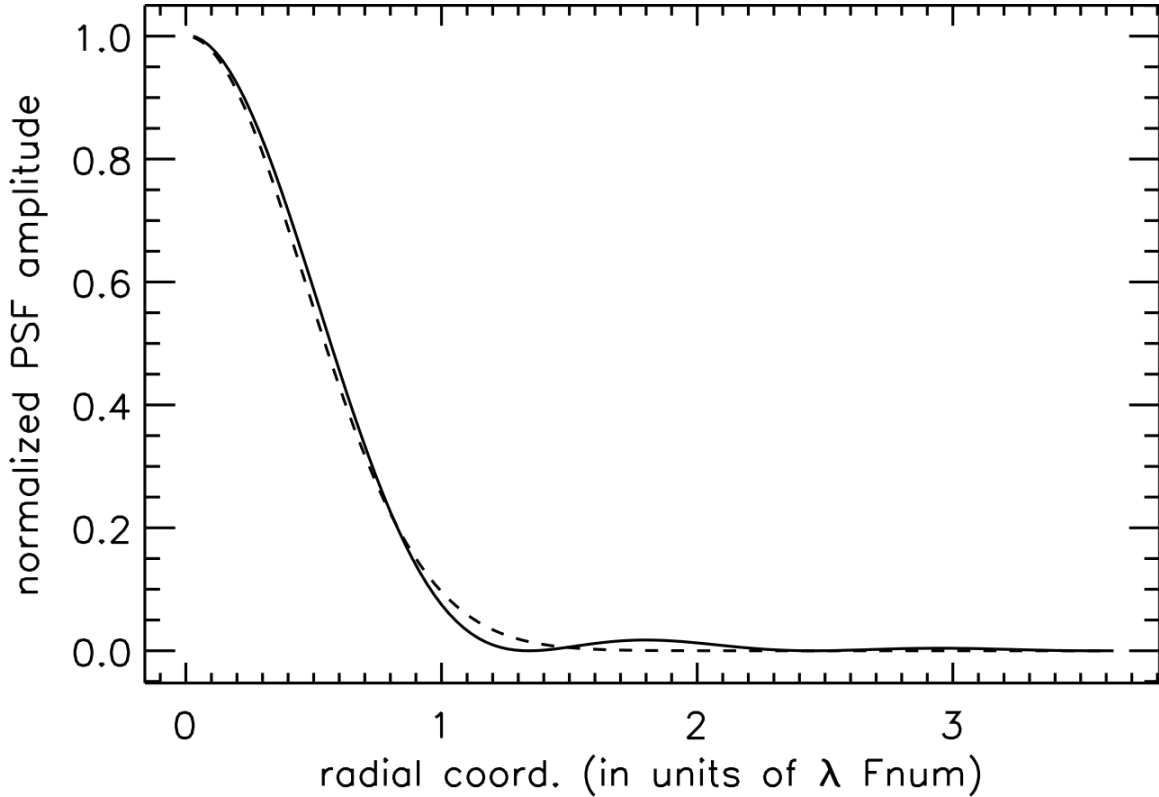


Figure 7. A Gaussian is superimposed above an Airy disk pattern with equal peak intensities. The x-axis represents the radial distance from the center of the distribution in terms of $\lambda \times f$ -number. Although the Gaussian is not normalized, the purpose is to illustrate the closeness of the curves to add justification that a Gaussian curve may be fit to a data set as an approximation when the data set is represented by an Airy Pattern.

In this approximation, the radial intensity distribution is instead given by

$$I(r) = I'_0 \exp\left(\frac{-r^2}{2\sigma^2}\right)^2 \quad (32)$$

with r being the radial distance from the center of the intensity distribution, I'_0 being the peak intensity, and σ being the RMS, or standard deviation for the Gaussian distribution. Similar to the method employed in finding an Airy pattern fit to our frames, by letting

$$r = \sqrt{(x - \bar{x})^2 + (y - \bar{y})^2}$$

we can plug our frame into Matlab's curve fitting toolbox with the fit equation being,

$$I(x, y) = I'_0 \exp\left(\frac{-((x - \bar{x})^2 + (y - \bar{y})^2)}{2\sigma^2}\right) + C \quad (33)$$

If I'_0 is set equal to the I_0 obtained from the Airy pattern fit, the vertical offset, C , should be approximately the same as well, and the σ that Matlab determines best fits a Gaussian to the frame being analyzed is our RMS. This yields one more method of determining where our focal spot is. By plotting the $1/\sigma$ against the transverse distance from the lens, where $1/\sigma$ is maximized, or σ is minimized, represents where the intensity distribution is tightest and where the focus is.

Zhang et al determined that the RMS of a Gaussian fit to a focal spot that can be approximated by an Airy pattern is

$$\sigma \approx 0.42\lambda N \quad (34)$$

Where N is the f-number of the lens. Fitting the frames to a Gaussian then, yields not only another method of finding the focus but another method beyond residuals of determining how well the pattern can be represented by an Airy.

The equation for the radius of the central lobe of an Airy pattern is given by the first zero of the Bessel function of the first order. The first zero of $J_1(r')$ occurs at $r' = 3.8317$. As Airy fit applied accounted for a horizontal spread, such that $r' = a \times r$, The actual radial distance for the fit applied would be $3.8317/a$. The location of this first dark ring is related to a lenses f-number by $1.22\lambda N$. Dividing the RMS of the

Gaussian fit with the radial distance to the first dark spot of the Airy pattern gives:

$$\frac{\sigma}{3.8317/a} = \frac{0.42\lambda N}{1.22\lambda N}. \quad (35)$$

Solving this for *sigma*, $\sigma = 1.3191/a$. If this equation is true when the fit values are plugged in, it would be further justification to approximate the spot intensity distribution by an Airy.

Strehl Ratio.

The Strehl ratio is a measure of how much wavefront aberrations from a spherical wave, affect image quality. The most desirable Strehl ratio is when there is no wave aberrations present, which yields a value of one. Before going in depth into the Strehl ratio, it is important to analyze the intensity distribution of a theoretically perfectly focusing circular lens. The perfect circular lens provides a focus in the shape of an airy pattern. The Airy pattern is obtained by squaring the Fourier transform of a circular aperture. As such, the size of the aperture, distance between the object and image plane, and radial distance along the image plane all play a role in the intensity obtained at any given point on the image plane. Particularly, after the Fourier transform is taken, the intensity distribution is given by: [5]

$$I(\theta) = I_0 \left(\frac{2J_1(ka \sin \theta)}{ka \sin \theta} \right)^2 \quad (36)$$

where a is the radius the circular aperture, $k = 2\pi/\lambda$, θ is the angle of observation, defined as the angle between the propagation axis from the center of the circular aperture to a spot on our observation plane, and J_1 is the Bessel function of order

one. This system can be seen in Figure 3. Simplifying Equation (36) and setting $r = k a \sin \theta$ gives:

$$I(r) = I_0 \left(\frac{2J_1(r)}{r} \right)^2 \quad (37)$$

The Strehl ratio then, is a measure of how good a focus is relative to the airy pattern. The strehl ratio is defined as the peak intensity of the focus of a lens, divided by the peak intensity that an airy pattern formed by a perfect lens would provide. In the case where intensity readings are not calibrated to absolute values, but an intensity profile is obtained, the following equation gives the normalized value of the peak intensity, relative to the peak intensity from the perfect focus, [5]

$$I(\sigma) \approx 1 - \left(\frac{2\pi}{\lambda} \right)^2 (\sigma)^2 \quad (38)$$

where σ is the RMS of the wavefront. This equation then, as it is normalized to the airy pattern, is also equal to the strehl ratio. Using Equation (38) is going to be one method used to analyze the performance of the lens discussed later on at its focus.

2.6 Nonlinear Optics

Nonlinear optics is the study of phenomena that take place due to the changing of the optical properties of materials when they are irradiated by high intensities of electromagnetic waves. These effects are considered nonlinear due to the fact that the response of the material system does not change linearly with a linear change in the magnitude of the incident electromagnetic wave. The difference in analyzing linear opposed to nonlinear properties comes from the polarization equation of the material. In Section 2.2, Equation (16) was used to describe the polarization of a

material. The full equation for a materials polarization is given as, [6]

$$\mathbf{P}^{\text{NL}} = \epsilon_0(\chi^{(1)}\mathbf{E} + \chi^{(2)}\mathbf{E}^2 + \chi^{(3)}\mathbf{E}^3 + \dots) \quad (39)$$

where $\chi^{(n)}$ is the n^{th} order nonlinear susceptibility tensor, and \mathbf{E} is the incident electric field. All of the susceptibility tensors with n greater than 1 are sufficiently small, that except for very large magnitudes for \mathbf{E} , all values except for the first product may be approximated as zero. At these large magnitudes, the nonlinear portion of the polarization leads to many different effects. Most of them being attributed to the $\chi^{(2)}$ and the $\chi^{(3)}$ effects, known as the second order non-linear effects, and third-order nonlinear effects respectively.

The interest in the lens studied in this thesis lies in its third-order nonlinear effect. In [6], it was shown that the second-order nonlinear contributions become zero for isotropic material. The two materials used are TiN(Titanium Nitride) and Al_2O_3 (Aluminum Oxide). TiN is the material that produces the focusing effect, and is deposited in such a manner onto the Al_2O_3 to be isotropic. [17], [18] As such, the second-order non-linear effects can be ignored, and an analysis of the lens performance can be focused on the third order effects.

Third Order Nonlinear Effects.

When the electric field strength is sufficiently large that the extra polarization terms cannot be approximated as zero, Equation (20) then becomes:

$$\epsilon_r = 1 + \chi^{(1)} + \chi^{(2)}\mathbf{E} + \chi^{(3)}\mathbf{E}^2 + \chi^{(4)}\mathbf{E}^3 + \dots \quad (40)$$

For this analysis, it was addressed that the second-order non-linear term becomes zero, and assuming that the effects from the 4th order and above non-linear terms

are still small enough to be negligible, it leaves,

$$\epsilon_r = 1 + \chi^{(1)} + \chi^{(3)} \mathbf{E}^2. \quad (41)$$

As discussed in Section 2.3, the refractive index of a material is given as:

$$n = \pm \sqrt{\mu_r \epsilon_r}.$$

The magnetic susceptibility of TiN is 4.7752×10^{-10} [12], [19], and from Equation (21), as χ_M is sufficiently small, we can approximate μ_r as 1. On one hand, with $\mu_r \approx 1$, it means that the sample will have both a reflective and transmissive focus and thus decreasing the amount of power in the transmissive focus; on the other hand, this μ_r simplifies the refractive index to $n = \sqrt{\epsilon_r}$, or, in this case,

$$n = \sqrt{1 + \chi^{(1)} + \chi^{(3)} E^2} \quad (42)$$

which can be expanded using a Taylor series expansion from

$$n = \sqrt{1 + \chi^{(1)}} \sqrt{1 + \frac{\chi^{(3)} E^2}{1 + \chi^{(1)}}} \quad (43)$$

to

$$n = \sqrt{1 + \chi^{(1)}} \left(1 + \left(\frac{\chi^{(3)} E^2}{2\sqrt{1 + \chi^{(1)}}} \right) / 2 + \left(\frac{\chi^{(3)} E^2}{2\sqrt{1 + \chi^{(1)}}} \right)^2 / 8 + \dots \right). \quad (44)$$

Assuming that $\chi^{(3)} E^2 \ll \sqrt{1 + \chi^{(1)}}$ so that the third term and beyond may be ignored allows the index to be split into the linear index, and nonlinear index parts such that

$$n = \sqrt{1 + \chi^{(1)}} + \frac{\chi^{(3)} E^2}{2\sqrt{1 + \chi^{(1)}}} \equiv n_0 + \Delta n \quad (45)$$

where n_0 is the linear index of refraction and Δn is the change to index due to non-linear effects.

The relationship between the intensity of an electromagnetic wave and its magnitude is equal to: [5]

$$I = \frac{1}{2}c\epsilon_0 n_0 E^2, \quad (46)$$

or solving for E^2 ,

$$E^2 = \frac{2I}{c\epsilon_0 n_0}. \quad (47)$$

This relationship allows leads to the introduction of the material's nonlinear refractive index and rewrite (45) as

$$n(I) = n_0 + n_2 I \quad (48)$$

with n_0 being predefined above as $\sqrt{1 + \chi^{(1)}}$, and n_2 being the mentioned nonlinear refractive index, equal to [6]

$$n_2 = \frac{1}{n_0^2 c \epsilon_0} \chi^{(3)}. \quad (49)$$

The fact that n_2 is directly proportional to $\chi^{(3)}$ confirms that the changes to the refractive index are, in fact, due to the third-order non-linearities. This revised refractive index, given by Equation (48) gets at the heart of the interest in analyzing the lens studied in this thesis and is one of the parameters of interest that will be reported.

2.7 Properties of Related Materials

The sample analyzed is a metasurface-lens designed by depositing cylindrical Titanium Nitride dielectric resonators onto a film of Aluminum Oxide. This section begins by addressing the properties of Titanium Nitride and Aluminum Oxide, then discusses the physics of using plasmonic resonators as meta-atoms in the fabrication of meta-lenses.

Bulk Properties.

The primary material of interest in this sample is Titanium Nitride (TiN). As mentioned, the meta-atoms on the metalens analyzed are constructed using this material. Titanium Nitride is very hard, tough, and temperature tolerant. [20] Combined with the fact that it has a low magnetic susceptibility, it makes it a perfect candidate for third-order nonlinear effect analysis. Its various properties are summarized in the Table 1 next to various other substances. It is important to note that compared to other common micro-resonating substances used meta-surfaces, such as gold and silver, TiN has a relatively very large thermal resistance and is very hard. Beyond the substance's surviveability, it is important to note its $\chi^{(3)}$ value of $-5.3 \times 10^{-18} [m^2/V^2]$ [3]. The goal is to show that the geometry of the metalens produces a larger effective χ^3 than the one inherent in the material itself.

Aluminum Oxide's (Alumina or Al_2O_3) strong ionic interatomic bonding gives rise to various desirable properties including its hardness and resistant to wear, its excellent broadband dielectric properties, its strength, and its good thermal conductivity. [21] All of these make Alumina ceramics an ideal choice for the substrate of a metasurface designed for optical frequencies, especially with desired third order nonlinear effect which require high intensities. [22] Alumina's nonlinear-index is two

orders of magnitude lower than that of Titanium Nitride as well, allowing the non-linear focusing effects to be dominated by the deposited TiN and the meta-lens it creates (applicable if not irradiated by collimated light, and when representing the entire sample as a refractive lens). The Thermal Resistance (TR), Dielectric Constant (DC) and Hardness can be summarized in Table 1. [23] [24] [21] [25] [19]

Beyond just the individual properties of *TiN* and Al_2O_3 , experimentally at high powers, *TiN* deposited onto Al_2O_3 produces a resonant quality factor (Q-Factor) in the *TiN* of over 10^7 , [26] [27] whereas in silver the Quality factor is maximized at around 75 and 18 for gold. [28] By choosing the resonators to be made of *TiN* rather than silver or gold then decreases the loss of energy in the nano-atoms.

Table 1. Summarizing Material Properties

Substance	TR at 20°C	DC	Hardness(knoop)
<i>TiN</i>	.03467	16.520	>2000
Al_2O_3	.03125	9.8	1440
<i>Au</i>	.003184	24.108	19.294
<i>Ag</i>	.002469	31.028	453

Meta-atoms Used: Plasmonic Resonators.

As mentioned, the meta-atoms used in the sample studied here are cylindrical plasmonic resonators. When these resonators interact with electromagnetic waves, the conduction electrons are driven in a collective oscillation along the length of the rod. These oscillations create changes to the incident electromagnetic field. The radiation from these nanoparticles then can be tuned (shape and direction) precisely due to the shape of the nanoparticles. As the radiation from these nanoparticles, make up the new wavefront, it is important for these nanoparticles to have a very specific geometry. For optical wavelengths, the most important relationship is that

the length of the rods is given by

$$L = \frac{n}{2} \lambda_{eff} \quad (50)$$

where L is the length, n is the index of the nanorod, and $\lambda_{eff} = n_1 + n_2 \frac{\lambda}{\lambda_p}$ where λ is the wavelength of the electromagnetic field and λ_p is the plasma wavelength. This is also known as the resonance condition. [29]

2.8 Focal Length Analysis

The primary purpose of analyzing this lens is determining how its focal length reacts to changes in intensities. As such, one of the most important decisions being made during this process is how to determine where the focus of the lens is. This section addresses the two methods used for this analysis.

Center of Focus.

When recording data, although the images obtained are roughly centered, for the methods that I will employ to determine where the focus of this lens is, I need to determine a more accurate estimation of the center. One method to determine the center of the intensity is to find the first moment of the image. Although in perfect symmetry, without any readout uncertainty, and with a perfectly centered image, this would result in the center of the focus. If the image of the focus is not perfectly centered, or the focus isn't symmetric in various directions, it has the potential to skew the moments. For the sample, rather than assuming perfect symmetry, and perfect data acquisition, for this analysis, a different method of image centering is used. Instead of centering the image on the center of intensity read outs at each slice, the center of the focus will be set to the point with the highest intensity readout. In all

measurements done that require analysis around the focus, this assumption will be made. Further justification for this is included in Figure 8.

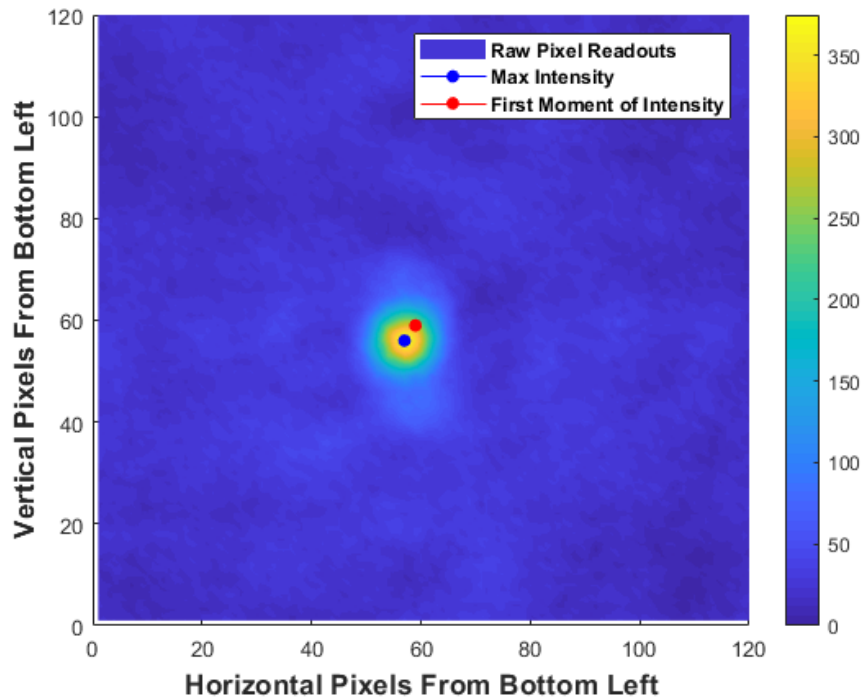


Figure 8. This figure is used to illustrate why the first moment of each slice is set to the location of the maximum intensity rather than of the calculated moment, which is clearly off center. This is just one example taken at an arbitrary slice, however the effect is present across all slices.

D4 σ .

Another method of focal analysis in beam propagation theory is analyzing the Second Moment, or the 4σ beam width. In this method, four times the standard deviation of an intensity profile is analyzed. In this analysis, the beam profiles spreads out in either direction of the focus and the smallest ' 4σ ' of the various z-distances scanned represents the focus. Using this, the second moments of each slice can be

calculated, to find the focus.

Rather than finding the second moment of the entire slice, it is more accurate to take the second moment about the peak intensity. Although calculating the first moment should yield that result, for reasons discussed in the “Center of Focus” section, instead of depending on the first moments then, the locations of the peak intensities will be used (as in the end the deviation around the focus is what is desired). For the x-direction, the center will be given as x_0 and likewise for the y-direction, the focus will be given by y_0 . These are plugged into a calculation of the variance about the peak intensity. The variance is a measure of how spread out the data is qualitatively, and quantitatively is the average of the squared distances from the center intensity. Assuming radial symmetry, [30]

$$\sigma_r^2 = \frac{\sum_r r^2 \times Z(r)}{\sum Z(r)} \quad (51)$$

where,

$$r = \sqrt{(x - x_0)^2 + (y - y_0)^2} \quad (52)$$

and Z represents the pixel readout at every location. From here, the 4σ is simply four times the square root of the obtained value. Plotting the obtained 4σ from each slice against the transverse distance from the lens, then finding the minimum of the 2-term fourier fitting curve is where the focus is. [31]

Power in a Bucket Method.

Although intensity was brought up when discussing the beam on the sample what causes the non-linear effects, for analyzing the focus, practically, detectors don't have infinite accuracy, so rather than reading out intensities, integrated intensities across a small area are reported. Given this, rather than intensities, what detectors measure is power. With this in mind, for the sake of distinguishing the power readouts, a hypothetical detector of radius approximately equal to the radius of the center lobe (at focus at low intensity), 8 pixels, will be used. Although a bucket size of 1 pixel could be used (peak pixel readout), expanding the area of the bucket eliminates some error that might be introduced due to the detector moving or slight variations in the beam or current supplied to the detector over the process of collecting data. In this analysis, all partial pixels were not included in the bucket. The focus should be where the readout is maximized, hence the maximum power is obtained. Rather than taking the maximum readout values however, from here, a fit can be applied to the data, and the slice closest to the largest power value represented on the best fit curve obtained will be the one representative of the focus.

In applying this method, the first step, beyond determining the bucket size, is determining the pixels that are all within a certain radius of the center of the focus. Using (52), after scanning across all pixel values that have x and y values that yield r values less than or equal to the determined bucket radius, are summed. The end result is a power with units of pixel counts. As all that matters is relative measurements, these units are fine. The slices can now be analyzed in the methods described in the preceding paragraph.

For the sake of this analysis, only that latter method will be used. Similar to the

$D4\sigma$ method, a Fourier Series with two terms will be fit to a plot of the maximum powers, and the peak value will be the determined focus for this method. [32]

Focal Dispersion Fitting.

The various properties discussed above, when plotted against z , produce a smooth pattern with the focus being at the extrema of the pattern. As such, a fitting curve is applied to the points and from there the extreme can easily be determined. Due to the fact that the second derivative of the parameters, or their concavity, are very different on either side of the extrema, a 2-term Fourier series is fit to the points, allowing both concavities to be accounted for when determining the extrema.

The form of the 2-term Fourier series fit in Matlab is reported as

$$Y = A_0 + A_1 \cos(\omega z) + B_1 \sin(\omega z) + A_2 \cos(2\omega z) + B_2 \sin(2\omega z) \quad (53)$$

where z is a transverse distance from the sample, ω is a fit frequency, and Y is the value of the parameters obtained from the analysis methods. From here, Matlabs[®] curve fitting toolbox determines the constants that best fit the curve to the data. The extrema of the resulting fit in the range of the data taken yields the location of the focus of the sample. Once this location is determined the various focal analysis techniques may be used on the appropriate slice to analyze how adjusting the beams power and wavelength affects the focusing of the sample.

Focal Separation.

Once the distance between extrema in dV is determined, that separation needs to be converted into microns. In order to calibrate the piezo motor to microns, the range in microns scanned needs to be known for one of the data sets. One of the focal points viewed is the first order diffractive focus, whereas the focus that is viewed when the microscope objective is closer to the metalens, is a virtual focus, and is the first order negative diffractive focus. [33] This can be understood by looking at Figure 9

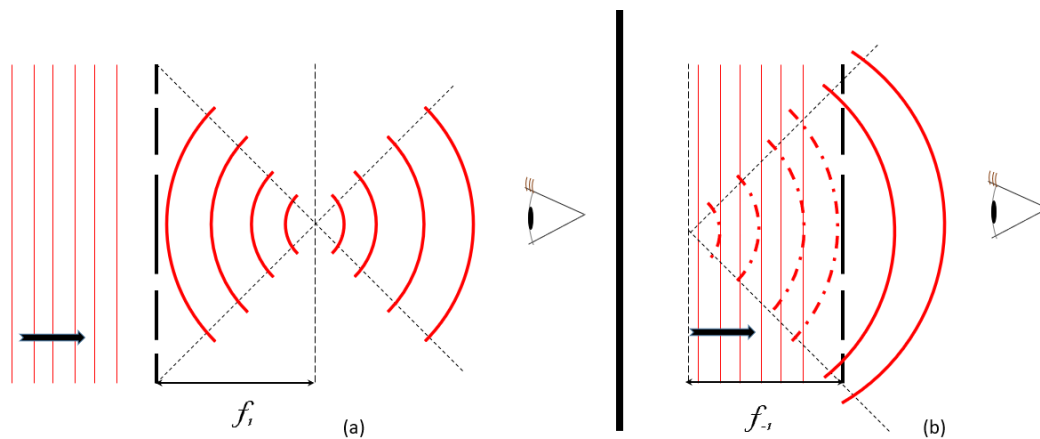


Figure 9. (a) The thin straight lines represent the collimated beam moving towards the diffractive optic. The thicker solid lines on the other end of the diffractive optic represent the effective resulting wave front after diffraction, leading to the observer (in this case, the microscope objective) (b) Similar to (a), when the observer is closer to the lens, they see effectively diverging waves that, if traced backwards, would lead to a focus equal to one focal length of the lens behind the lens. The dashed thick red lines represent the virtual wavefront from behind the lens.

As the first order diffractive focii (positive and negative) are equally spaced from the lens, and assuming that the lens is designed to focus at 10 microns for low power, setting the separation between observed focii to 20 microns allows for the calibration of the piezo motors positioning in terms of dV .

2.9 Focal Analysis

Beyond determining where the focus is for this metalens, it is desirable to know how the nonlinear effects and changes in wavelength affect these metalenses, so further analysis will be done to intensity profiles. The three methods of analysis are addressed in this section.

Airy Fit.

As discussed in Chapter 2.4, although this lens is not a perfect circular lens, comparing the shape of the intensity profile to the shape of an airy pattern could be quantitatively informative to the shape and behavior of the focus, and is informative as to how close it is to producing the shape of a focus obtained from a perfect circular lens.

In this analysis, after the location of the focus is determined for each intensity and wavelength scan, the slice closest to that focus is used. A square window that encloses approximately three times the width of the central lobe is fit to an airy pattern. In order to fit each focal slice to an airy pattern, there are a few manipulations to be done to Equation (37). First, there is some base offset that needs to be taken into account, as well as some radial stretching of r . Each slice is also broken down into x and y coordinates as opposed to radial coordinates. Letting a be the radial stretching factor on r , C be the vertical offset, and letting

$$r = \sqrt{(x - x_0)^2 + (y - y_0)^2} \quad (54)$$

where x_0 and y_0 are used to center the airy pattern, the function that each slice is fit

to is:

$$I(x, y) = I_0 \left(\frac{2J_1(a\sqrt{(x-x_0)^2 + (y-y_0)^2})}{a\sqrt{(x-x_0)^2 + (y-y_0)^2}} \right)^2 + C. \quad (55)$$

This function is plugged into M[®] curve fitting toolbox with M[®] solving for all variables that would give the best fit. After applying this analysis to each slice, the resulting R^2 values are recorded. This process is applied only to each focal plane. By comparing the resulting R^2 values along the positive first order diffraction focal pairs, is informative as to how the shape changes for each focus and which more closely resembles and airy pattern. Comparing these pairs across the other intensities and wavelengths then is a way of comparing how the shape of the focus is affected by intensity and wavelength.

Strehl Ratio Analysis.

An effective Strehl Ratio analysis between focii can be done fitting curves to an airy pattern in the manner that the maximum intensities obtained can be compared. Rather than just comparisons relative to other scans, however, Equation (38) gives a method of obtaining true values for the Strehl Ratio relative to a perfect circular lens. As this lens operates purely based off of diffraction, because the wave does not travel through a bulk material, but rather is absorbed by many small antenna and re-emitted, it should have a relatively high Strehl Ratio, however as the engineered phase profile only contains two unique phase adjustments, this may hurt the Strehl Ratio. The Rayleigh Limit is an accepted standard of optical quality. The Rayleigh limit at its core is a standard of the amount of wavefront deformation of an image at its focus that is acceptable. It was determined that as long as the deformation

corresponded to a $1/4$ wave or less, the image was perceived as approximately perfect. This deformation corresponds to a Strehl Ratio of 0.82, and as such, this Strehl Ratio is the Rayleigh Limit. [34] The metalenses performance will be compared to this standard based on Equation (38).

Power in Bucket at Focus.

In applying this method, the bucket size is going to be a constant and the width of the bucket will be set equal to what is observationally approximately the total width of the primary at low intensities, corresponding to 16 pixels in this case. The pixel counts will all be summed together yielding a power value in terms of $[counts/m^2]$. As discussed earlier, as for this analysis, the comparison that matters is relative measurements between the two foci in each scan, so non-metric units are fine. The peak power values along the fitting curves for each scan are taken and used to compare to the other scans.

The primary takeaway from this analysis is determining the relative power in the negative primary diffractive focus when compared to the positive primary diffractive focus of the sample.

2.10 Index Analysis

Refractive Lens Analysis.

The modeling of metalenses as a refractive lens creates effective radii of curvatures, as well as indexes of refraction that can be plugged into the lens maker's formula given by:

$$\frac{1}{f} = (n - 1) \left(\frac{1}{R} - \frac{1}{R'} \right) \quad (56)$$

Where f is the focal length of the lens, n is the refractive index of the lens, and R and R' are the radii of curvature of both sides of the lens. [12]

There are two methods that may be used in solving for the effective index of refraction. The first would be to assume the effective lens' non-linear index is equal to that of the material of which the meta-atoms are made. This then allows one to solve for the lens' effective radii, $(\frac{1}{R} - \frac{1}{R'})$. After the effective radii are known, the intensity of the incident electromagnetic waves can be ramped up to the point that nonlinear effects take effect. At this point Equation (56) becomes

$$\frac{1}{f} = (n_0 + n_2 I - 1) \left(\frac{1}{R} - \frac{1}{R'} \right). \quad (57)$$

Solving for n_2 then yields

$$n_2 = \frac{1/f - (n_0 - 1)(\frac{1}{R} - \frac{1}{R'})}{I(\frac{1}{R} - \frac{1}{R'})}. \quad (58)$$

The benefit for solving in this method is that n_2 can then be compared to that of a lens made purely of TiN and the change in the n_2 due to the geometry and machining can effectively be obtained. The downside to this method is that it assumes the lens, in this geometry, would have a linear index of refraction equal to that of its corresponding lens made of the same material.

An alternative measurement of the lens characteristics is to, rather than assume the effective n_0 of the lens in order to solve for the lenses 'effective radii', I will define two new parameters:

$$n_{ml} = (n_0 - 1) \left(\frac{1}{R} - \frac{1}{R'} \right) \quad (59)$$

$$n_{mnl} = n_2 \left(\frac{1}{R} - \frac{1}{R'} \right), \quad (60)$$

with n_{ml} representing the meta-linear refractive index, a property inherent to the lens made when the lens is treated as a refractive optic. Conversely, n_{mnl} is the meta-nonlinear refractive index, similar to the n_{ml} , it is a characteristic of the lens that describes how the metalens focuses, while being treated as a refractive optic. Both n_{mnl} and n_{ml} have dimensions of $1/m$. This allows the lens makers formula to be written as:

$$\frac{1}{f} = n_{ml} + n_{mnl}I. \quad (61)$$

Although this method of analyzing the lens doesn't make for very effective comparison against non-meta lenses, it does give a straightforward property that can be assigned to each manufactured lens, and as a library of n_{ml} and n_{mnl} is compiled, patterns may be beneficial in telling more about the properties of metalenses.

In this analysis, both methods of index analysis will be performed, and values for n_2 , n_{ml} , and n_{mnl} will be reported.

Zone Plate Analysis.

An alternate method of analyzing this lens is by comparing it to that of a phase reversal zone plate. By creating a profile that would be the phase zone plate equivalent of the metalens analyzed, in the manner described in Chapter 2.5, rather than assuming the index of the lens in nonlinear regimes, the index may be solved for.

This results in an index that is much higher than that of TiN. From here, using 48, once the other effective refractive index values are solved for at higher intensities, the nonlinear indices can also be solved for. Both the low power index, and nonlinear index will also be reported using this method of analysis.

III. Design and Methodologies

3.1 Lens Design

The meta lenses used in this experiment are created by depositing Titanium Nitride onto an Aluminum Oxide substrate. For the sample being analyzed, through the use of various genetic algorithms, the deposited locations are determined in such a manner that at low intensities, incoming electromagnetic waves with wavelengths of 800nm will focus at 10 microns. The lens design is represented in Figure 10 [2], with an image of the lens being shown in Figure 11.

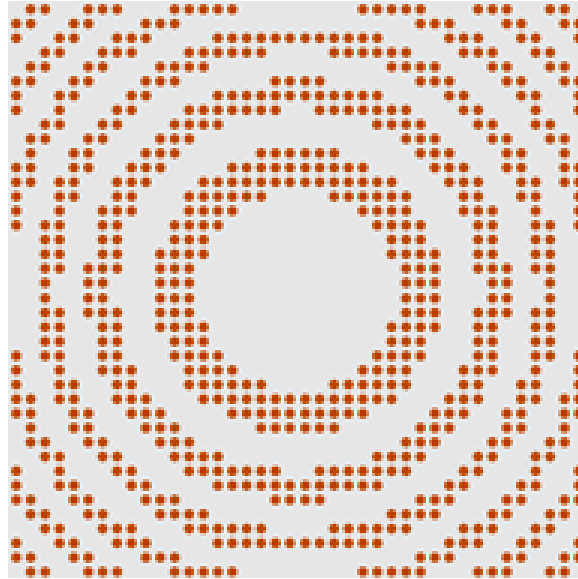


Figure 10. Red dots represent the TiN deposits. This Figure shows the pattern of the TiN lens that we are analyzing. This is the design of the desired sample rather than what is actually manufactured.

3.2 Lab Setup

The laser used in this system is a Griffin-5 tuneable oscillator. To get the most power in the output beam as possible, the oscillator is pumped 10W beam. The

output beam with this pump power yields 676 mW of power illuminating the sample, measured right before the beam is incident to the metalens. From the Griffin-5 oscillator, the beam travels through a variable neutral density filter used to view the focus at lower energies without changing the shape of the pulses. Before the pulse enters the NSOM (Near Field Scanning Optical Microscope) hood, the pulse is checked with an APE Mini autocorrelator to determine the pulse width as closely as possible to the sample. A diagram of the autocorrelator is given in Figure 12.

Once in the NSOM hood, the beam travels through two 5.7 cm focusing bi-convex lenses. These lenses are kept at 11 cm apart, and given Equation 52, this tells us that the focal length of this system is 81.2 cm. This is illustrated in Figure 13

$$f_{eff} = \frac{f_1 \times f_2}{f_1 + f_2 - d} \quad (62)$$

where f_{eff} stands for the system's effective focal length, f_1 and f_2 are the focal lengths of each of the lenses, and d is the distance between them. [35]

Although the lenses were designed to focus a planar collimated beam, relative to the focal length of the lenses, and relative to the distances being analyzed, the beam curvature at its focus on the sample is approximately flat. As these lenses cause chirping of the beam, and the pulse width is measured before the laser passes through the lenses, to get an accurate estimation of the pulse width at the sample, the pulse width before both lenses was inserted into the dispersion equation:

$$\Delta\tau = |D_v|\Delta v z \quad (63)$$



Figure 11. The copper colored dots represent the actual Titanium Nitride deposited onto the Alumina substrate. All of these together combine to make the metalens being analyzed. The lens is 10 microns wide and long.

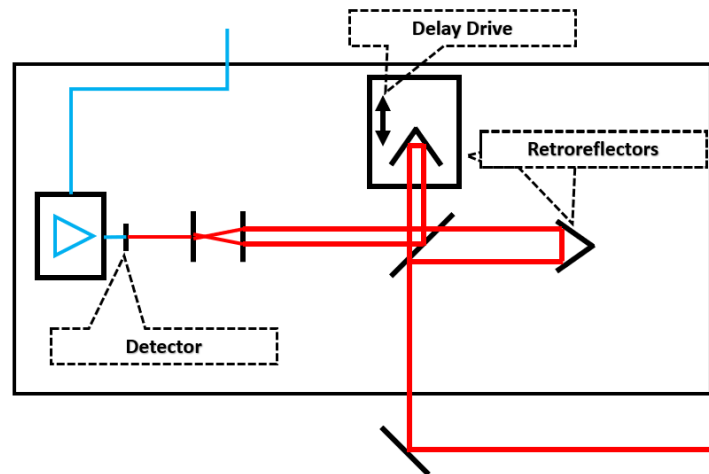


Figure 12. A basic diagram for the autocorrelator used to determine the pulse width. The beam enters from the bottom of the diagram and is incident to a beam splitter. One path of the beam hits a retroreflector and shines straight through to the detector. The other beam is incident on a retroreflector inside a delay drive that rapidly increases and decreases the beam path. The reflection rejoins the other path and is autocorrelated with it on a detector.

twice, to find that at the sample, the pulses are 141 femto seconds wide. [36] In Equation (63), $\Delta\tau$ represents the change in the pulse width, D_v is the dispersion coefficient of the material, Δv is the spectral width in FWHM, and z is the width of the material through which the beam is passing. The next step to determining the intensity at the sample is determining the shape of the pulse irradiating it. Assuming that the pulse is shaped well from the oscillator, it will have an approximately Gaussian intensity profile at the sample. [5] The general form for the normalized intensity distribution of a Gaussian is given as

$$I/I_0 = \exp\frac{-2r^2}{\omega^2} \quad (64)$$

with r being the radial distance from the center, and ω being the beam radius. At the focus, the beam radius is called the beam waist and is equal to $1/e^2$ with the same units used for r . With the system set up such that the beam is hitting the sample at the beam waist, and when measuring the power distribution where the sample was, all points varied to small degrees, but all normalized pixel values read out above .8. Solving for the radius that the sample was within the beams center then can be done by setting the left hand side of Equation (64) equal to 0.8. This gives an r value equal to 1.2288. Integrating Equation (64) then from 0 to 1.2288 yields 0.2305. This shows that about 23.1 percent of the power is within the area within which the samples were measured. Assuming that, because the variation in power distribution on the lens was less than 10 percent, the sample was uniformly irradiated, gives the power distribution as:

$$P_{sample} = 0.230534P_{total} \quad (65)$$

The area in which the beam's power was above 80 percent max intensity had ap-

proximately a $15 \pm 2\mu m$ radius. From here, with f representing the pulse repetition rate, A representing the beam's spot size, and τ being the pulsewidth, the intensity at the sample can then be seen to be

$$I = \frac{0.2305P_{total}}{f \times \tau \times A} \quad (66)$$

In order to scan and determine the focal length of the microlenses, the sample is placed on a piezo stage and scan it up and down relative to the microscope objective using a Nanonics piezo stage in intervals of what is determined to be 0.0309 microns. At each location, 1000 pictures of the microscopes focal plane are taken, and each pixel is averaged over the readings to get a more accurate reading of the focal planes at each point. Given the spot size of the laser, the Rayleigh range of this beam is 9.8mm. Relative to this Rayleigh range, given that the scans view a range of 20 microns, three orders of magnitude less, the intensity of the laser on the sample is assumed to be constant with respect to z .

With the exact location of the sample being hard to detect, measurements of both of the focal spots are taken through scanning the sample on the piezo in the manner shown in Figure 14. Given that the two focal points viewed are the positive primary diffractive focus and the negative primary diffractive focus, and the distances of each from the sample are equal, the distance between the focii is equal to

$$d = f_{+1} + f_{-1} = 2f \quad (67)$$

where the d is the distance between the focii, f_{+1} is the positive primary diffractive focal length, and f_{-1} is a negative primary diffractive focal length. constant accounting

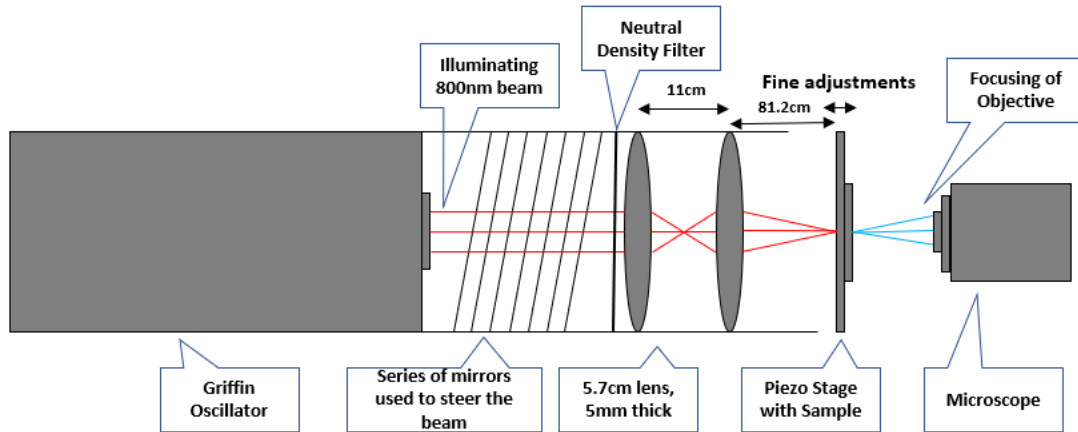


Figure 13. This figure illustrates the path of the beam as it progressing from the Griffin Oscillator to the sample, and through it to the microscope

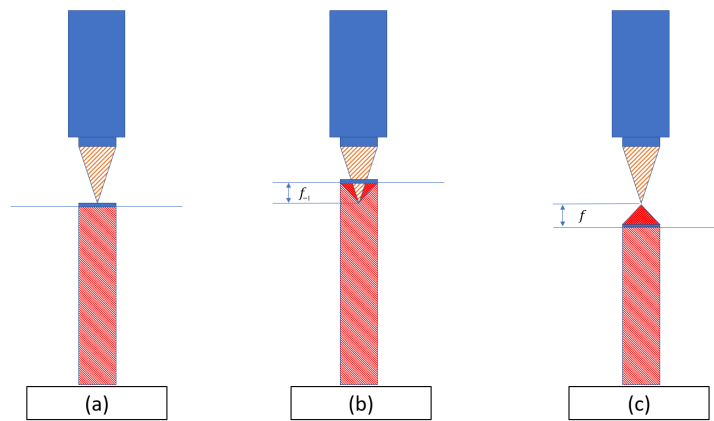


Figure 14. (a) The blue figure at the top represents our microscope objective, the orange triangle represents where the objective is focusing, and the red pillar represents the laser light coming in from below. In this figure, the microscope is viewing strictly the sample. (b) The red triangle represents the virtual diverging virtual rays that cause the effect of viewing a focus behind the lens. (c) In this figure, the objective is viewing the rays that create the primary positive diffractive focus.

for the tightening of the focal length.

3.3 Data Acquisition

In order to obtain as accurate data as possible to where the focal location of the lens is, a 100X objective was used in taking all of the data. For each finite distance away from the sample measured (z-slice), one thousand pictures were taken of the microscopes output. The exposure is adjusted until when scanning past the focus, none of the pixels from the camera are saturated. The camera measures in red, green and blue and reports values of each in every pixel.

When analyzing the data and determining which pixel has the maximum value, all three RGB values are summed. A Matlab[®] script scans each image and saves the maximum value for each. Once the relative locations of the focuses of varying power were determined, the exact distance of the focus can be found by setting the relative distance between the two focii at low illumination to 20 microns, as the microlenses were designed to focus at 10 microns at low intensities. The relative distances of the focii are then scaled at high intensities proportional to the results obtained from the lower power illumination.

IV. Results and Analysis

4.1 Data and Graphs

Plugging in each data set separately into Matlab[®] gives fit estimations of where the focus is located. When determining the location of the focus, the voltage input to the piezo stage were adjusted by a tenth of a voltage at a time. The various methods discussed in Section 2.6 are then used to obtain a property of the intensity distribution of each slice. When these properties are plotted against z , the concavity of the resulting curve is significantly different on either side of where the focus should be. As the concavity changes, the resulting curve is fit to a 2 term Fourier series given by Equation (53), which allows both concavities to be taken into account when determining the extrema of the curves.

This gives the location of the focus in terms of the voltage input into the piezo. As discussed in Section 2, the voltage difference at 800 nm at the lowest power is assumed to be equal to $20\text{ }\mu\text{m}$. This calibration is applied to all scans, and by averaging the distance between both focii at each slice, the location of the focii at various power levels is found, and the resulting behavior around the focus is plotted.

Various analysis methods are applied to the beam as discussed in Section 2.6 to determine how the intensity and wavelength changes affect the focal spots. In moving towards determining the effective n_2 value of this micro lens, the remaining beam characteristics are first calculated in order to get the intensity on the sample.

Filling in applicabke values for Equation (63), the dispersion coefficient for glass is $-131.42\text{ps}/(\text{nm}\cdot\text{km})$ [19], the spectral width is 25 nm , and our lenses being 0.000005km wide, the chirp caused by each lens to the FWHM is $.016\text{ps}$, or equivalently, 16fs .

Using an APE Autocorrelator, the beam can then be scanned and get the pulsewidth of the beam prior to two lenses to be 108 fs, leading to the pulse width that is incident on this sample to be 141 fs. After plugging both the power values into Equation (66), the intensity values reported in Table 2 are obtained:

Table 2. Reporting the Intensities for the Powers and Wavelengths Scanned

Wavelength(nm)	Power(mW)	Intensity(MW/cm ²)
800	679.81	16.93
800	187.10	4.66
800	27.16	0.68
760	32.86	0.82
840	21.67	0.54

4.2 Focal Shift Across Scans

In all of the methods to be described, the reported values are in terms of the piezo movement from when the microscope focus is on the sample itself. Negative values represent the microscope is viewing below the sample (to see the virtual primary focus), and positive values indicate the microscope is viewing above. Both primary diffractive focii (positive and negative) should be the same distance from the sample for the reasons mentioned above, however due to the increasing intensity on the sample, nonlinear effects begin to tighten that separation. The methods to be discussed in this section are $D4\sigma$ and Power in a Bucket method, and analysis of those results.

$D4\sigma$.

The first set of data analyzed was group taken at 800nm at low power. The usefulness in this is, excluding nonlinear focusing effects, the lens was designed to focus at 10 microns, so as the z axis is not calibrated to the sensor, this allows for a first step of calibration. By using the assumption described in Section 3, the distance

between foci in volts is set equal to $20\mu\text{m}$. This calibrates the piezo motors in the z direction.

The lowest power scanned while the laser's spectrum was centered at 800nm was $27.16 \pm 0.76\text{mW}$. Using Equation (66), this gives an intensity on the sample of $0.6761\text{W}/\text{cm}^2$. The sample was then scanned along the z direction, and in the method described in Chapter 2, the slices $D4\sigma$ were determined and plotted against z. After fitting Equation (53) to the $D4\sigma$ values, the results are plotted in Figure 15.

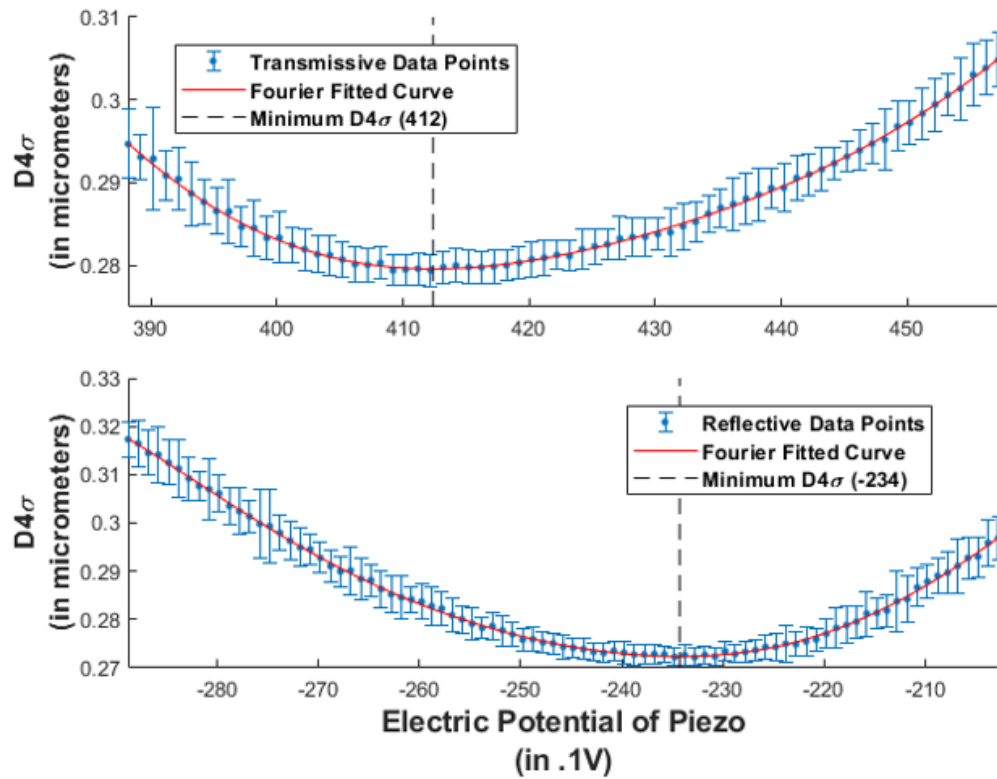


Figure 15. Illustrated is the $d=4$ Sigma values obtained when scanning near the foci for the sample illuminated with a beam of bandwidth centered at 800nm with a 25nm FWHM. After progressing through a neutral density filter, the power of the beam is 27.16mW, and the intensity at the sample is approximately $0.6761\text{MW}/\text{cm}^2$. Using the methods discussed in the Subsection “ $D4\sigma$ ” in Section 2.7, an array of $D4\sigma$ values are obtained for varying voltage readouts of the z-piezo motor near the focus of the sample. The results near the positive diffractive focus of the metalens are on the top, with the negative diffractive focus results being on the bottom. The minimum of the fitted curve is given by the dashed line.

The minima of the fitting curves are at $32.51V$ and $-32.15V$. Calibrating the piezo motors from this focal length and setting it to $10\mu m$ shows the piezos move at $0.309\mu m/dV$. Correcting the axis for this calibration and centering the difference yields Figure 16.

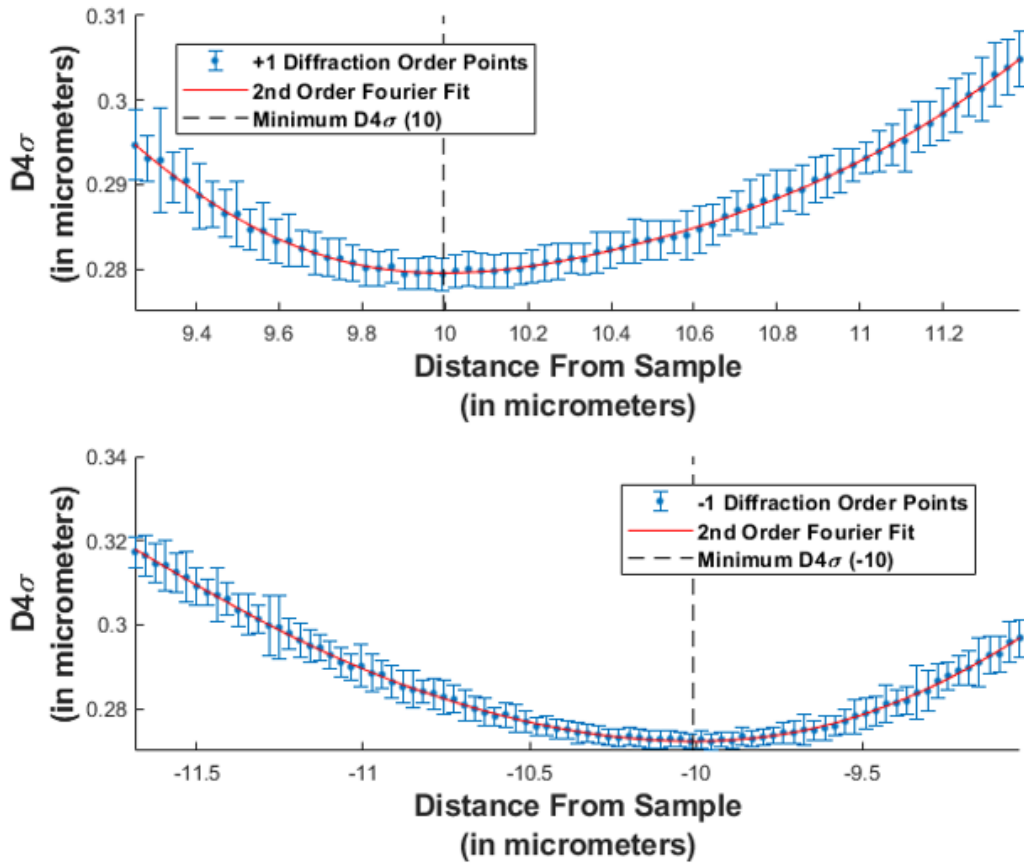


Figure 16. Illustrated is the $d=4$ Sigma values obtained when scanning near the foci for the sample illuminated with a beam of bandwidth centered at $800nm$ with a $25nm$ FWHM. After progressing through a neutral density filter, the power of the beam is $27.16mW$, and the intensity at the sample is approximately $0.6761MW/cm^2$. Using the methods discussed in the Subsection “ $D4\sigma$ ” in Section 2.7, an array of $D4\sigma$ values are obtained for varying voltage readouts of the z-piezo motor near the focus of the sample. The results near the positive diffractive focus of the metalens are on the top, with the negative diffractive focus results being on the bottom. The minimum of the fitted curve is given by the dashed line.

After the z-location in the piezo is calibrated, more measurements can be taken. Figures 17 through 20 provide the rest of the scans done using this method. These

results obtained from these scans are summarized in Table 3.

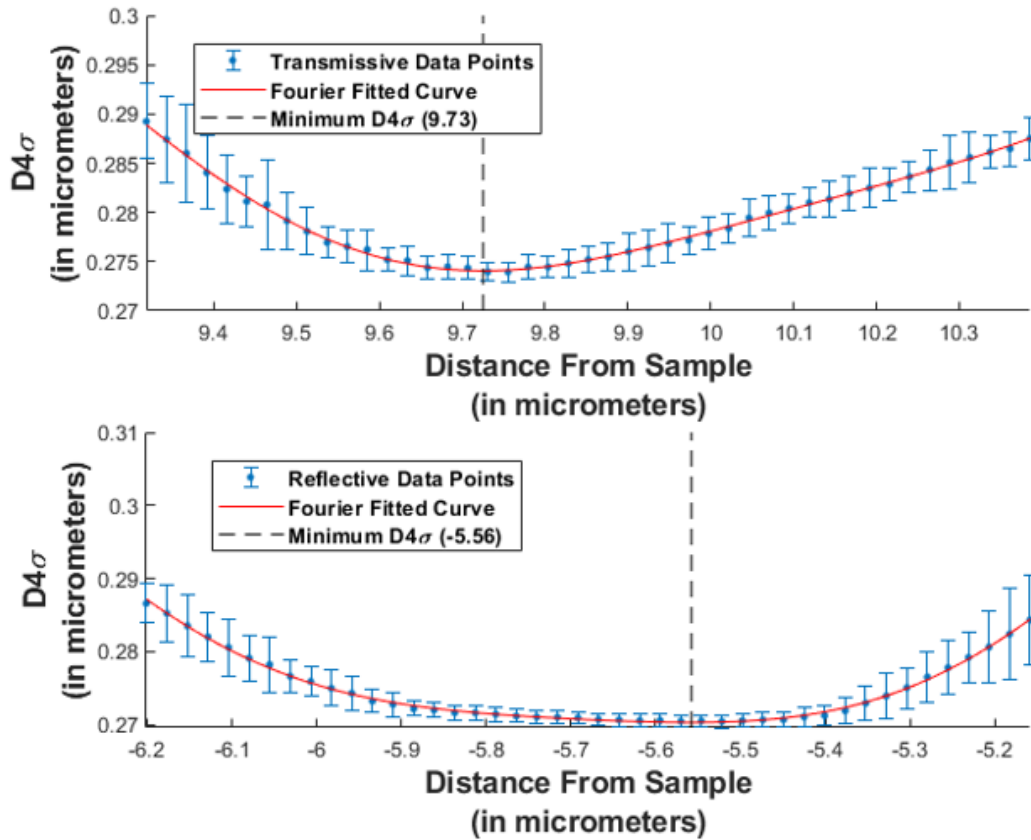


Figure 17. Illustrated is the $d=4$ Sigma values obtained when scanning near the foci for the sample illuminated with a beam of bandwidth centered at 800nm with a 25nm FWHM. After progressing through a neutral density filter, the power of the beam is 187.1mW, and the intensity at the sample is approximately 4.658MW/cm². Using the methods discussed in the Subsection “ $D4\sigma$ ” in Section 2.7, an array of $D4\sigma$ values are obtained for varying voltage readouts of the z-piezo motor near the focus of the sample. The results near the positive diffractive focus of the metalens are on the top, with the negative diffractive focus results being on the bottom. The minimum of the fitted curve is given by the dashed line.

Table 3. Reporting Focal Distances of Each Scan for $D4\sigma$ Fit

Power(mW)	λ (nm)	Intensity(MW/cm ²)	Focal Length(μ m)
679.8	800	16.93	9.650 \pm .003
187.1	800	4.66	9.728 \pm .005
27.16	800	0.68	10.000 \pm .007
32.86	760	0.82	10.572 \pm .004
21.67	840	0.54	9.208 \pm .005

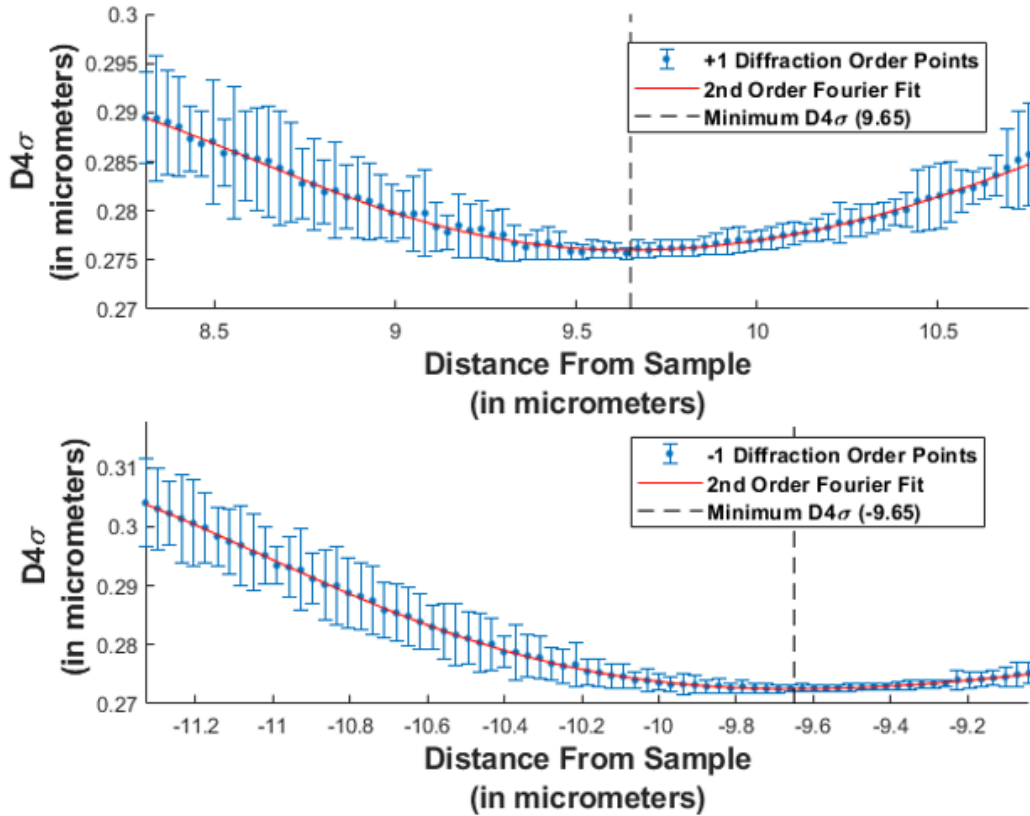


Figure 18. Illustrated is the $d=4$ Sigma values obtained when scanning near the foci for the sample illuminated with a beam of bandwidth centered at 800nm with a 25nm FWHM. After progressing through a neutral density filter, the power of the beam is 679.8mW, and the intensity at the sample is approximately 16.93MW/cm². Using the methods discussed in the Subsection “ $D4\sigma$ ” in Section 2.7, an array of $D4\sigma$ values are obtained for varying voltage readouts of the z-piezo motor near the focus of the sample. The results near the positive diffractive focus of the metalens are on the top, with the negative diffractive focus results being on the bottom. The minimum of the fitted curve is given by the dashed line.

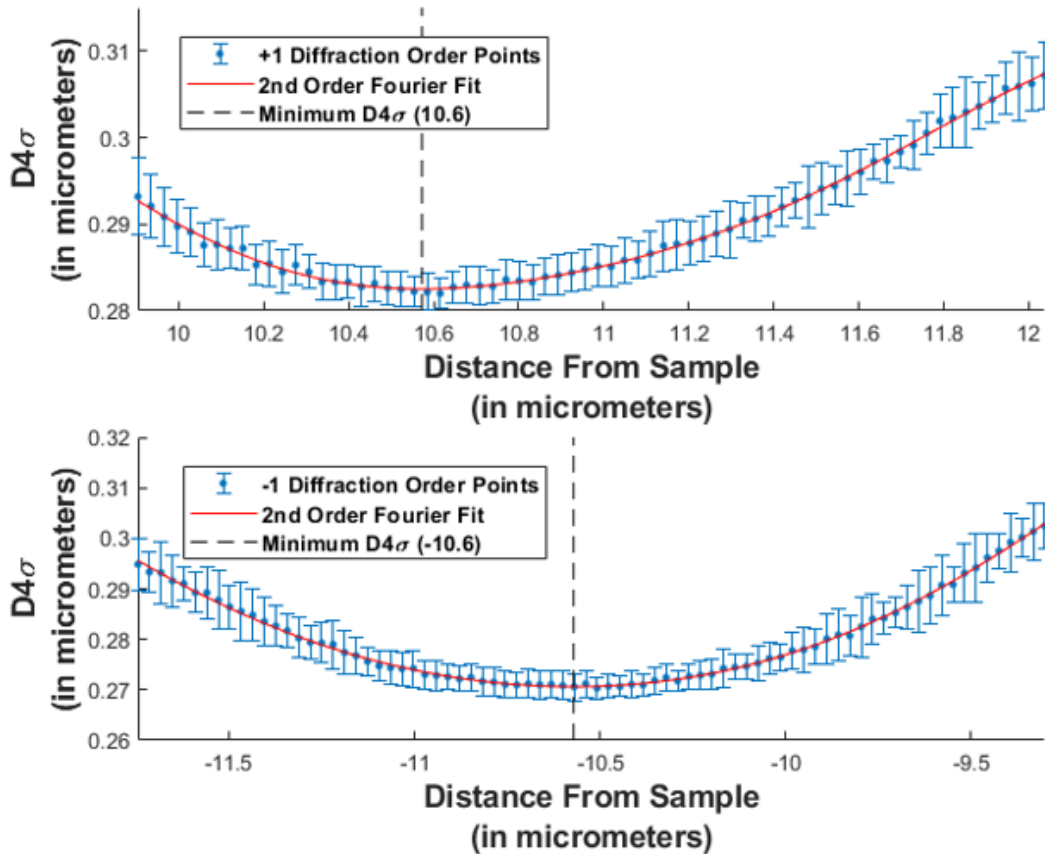


Figure 19. Illustrated is the $d=4$ Sigma values obtained when scanning near the foci for the sample illuminated with a beam of bandwidth centered at 760nm with a 25nm FWHM. After progressing through a neutral density filter, the power of the beam is 32.863mW, and the intensity at the sample is approximately 0.818MW/cm². Using the methods discussed in the Subsection “ $D4\sigma$ ” in Section 2.7, an array of $D4\sigma$ values are obtained for varying voltage readouts of the z-piezo motor near the focus of the sample. The results near the positive diffractive focus of the metalens are on the top, with the negative diffractive focus results being on the bottom. The minimum of the fitted curve is given by the dashed line.

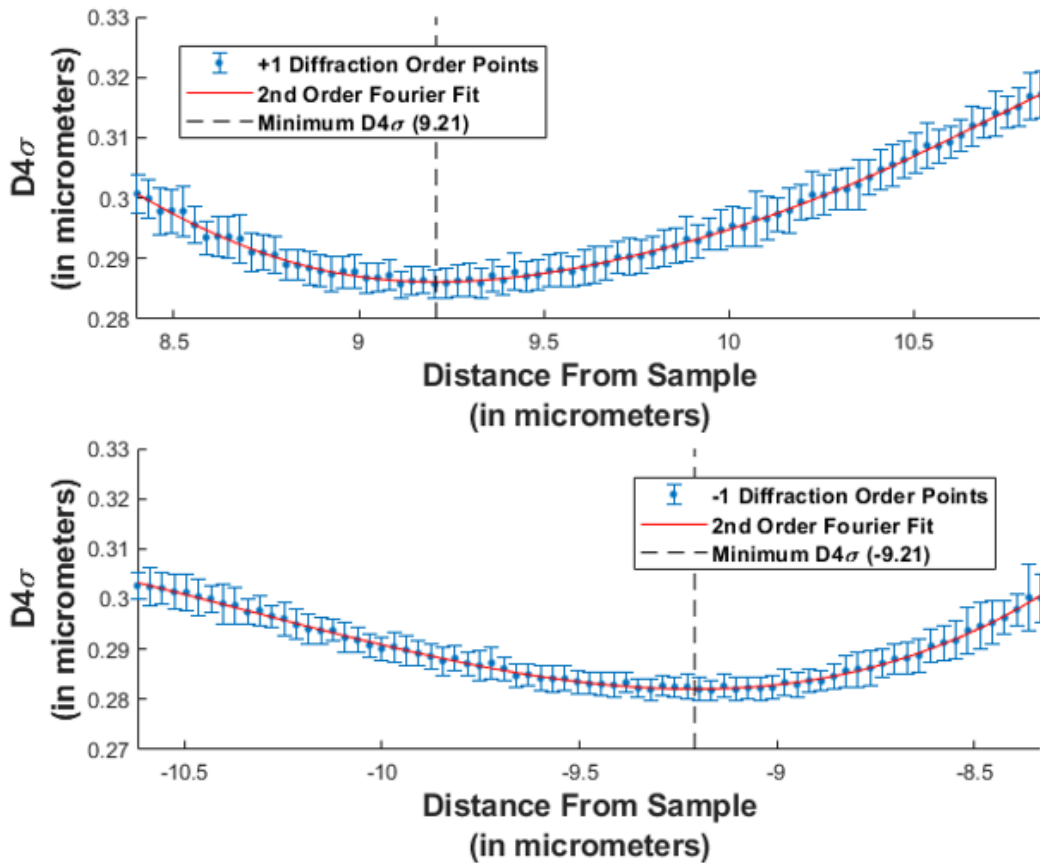


Figure 20. Illustrated is the $d=4$ Sigma values obtained when scanning near the foci for the sample illuminated with a beam of bandwidth centered at 840nm with a 25nm FWHM. After progressing through a neutral density filter, the power of the beam is 21.67mW, and the intensity at the sample is approximately 0.540MW/cm². Using the methods discussed in the Subsection “ $D4\sigma$ ” in Section 2.7, an array of $D4\sigma$ values are obtained for varying voltage readouts of the z-piezo motor near the focus of the sample. The results near the positive diffractive focus of the metalens are on the top, with the negative diffractive focus results being on the bottom. The minimum of the fitted curve is given by the dashed line.

Power in a Bucket.

Just as with the $D4\sigma$ analysis, the first set of data analyzed was taken at 800nm at low power, and for the same reasons the resulting extrema were used to calibrate the z-direction for this method.

The lowest power scanned while the lasers spectrum was centered at 800nm was $27.16 \pm 0.76mW$. Using (66), this gives an intensity on the sample of $0.68MW/cm^2$. The sample was then scanned along the z direction, and in the method described in Section 2, a bucket with a diameter of 16 pixels was used, and the power in the bucket for each slice was plotted against z. After fitting (53) to the "Power in a Bucket" values, the results are plotted in Figure 21

The minima of the fitting curves are at $33.33V$ and $-32.00V$ respectively. Calibrating the piezo motors using this focal length and setting it to $10\mu m$ shows that the piezos move at $0.306 \pm .001\mu m/dV$. Correcting the axis for this callibration and centering the difference yields Figure 22

After the z-location in the piezos is calibrated, more measurements can be taken. Figures 23 through 26 provide the rest of the scans done using this method. These results obtained from these scans are summarized in the Table 4.

Table 4. Intensity and Focal Length Reports for Scans across Power and Wavelength

Power(mW)	λ (nm)	Intensity(MW/cm ²)	Focal Length(μm)
679.8	800	16.93	$9.647 \pm .013$
187.1	800	4.66	$9.799 \pm .003$
27.2	800	0.68	$10.000 \pm .006$
32.9	760	0.82	$10.480 \pm .011$
21.7	840	0.54	$9.214 \pm .014$

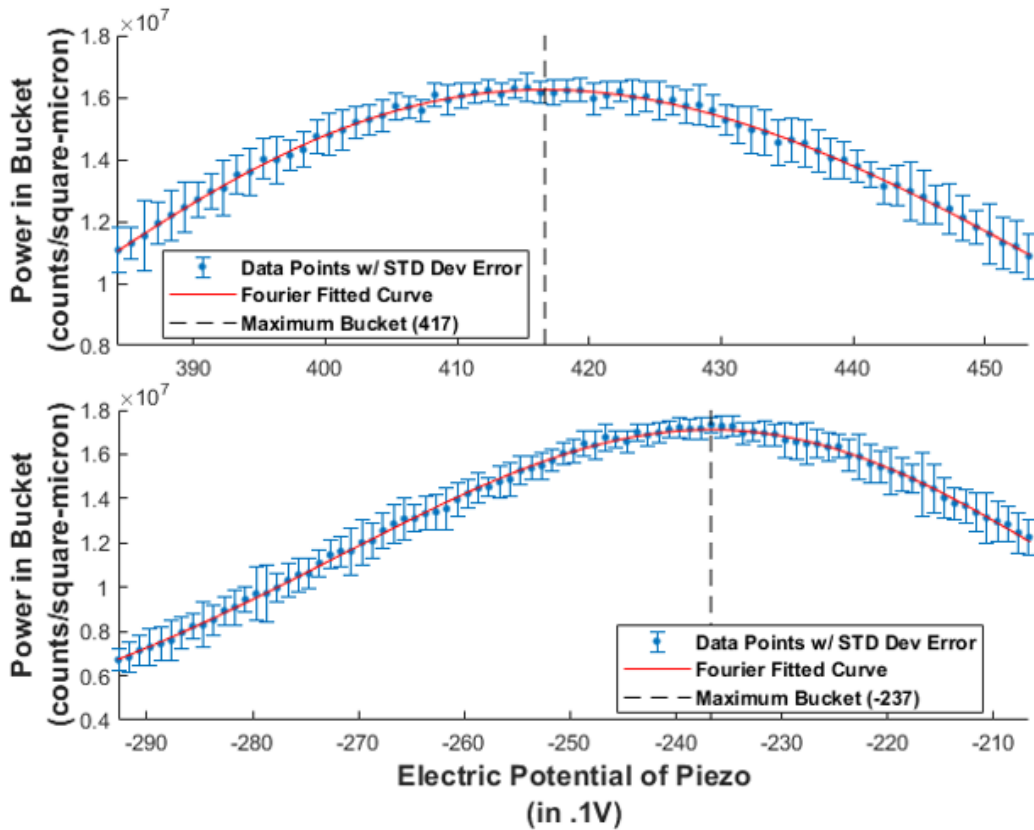


Figure 21. Illustrated is the Power in a Bucket values obtained when scanning near the foci for the sample illuminated with a beam of bandwidth centered at 800nm with a 25nm FWHM. After progressing through a neutral density filter, the power of the beam is 27.16mW, and the intensity at the sample is approximately 0.6761MW/cm². Using the methods discussed in the Subsection “Power in a Bucket Method” in Section 2.7, an array of Power in a Bucket Method values are obtained for varying voltage readouts of the z-piezo motor near the focus of the sample. The results near the positive diffractive focus of the metalens are on the top, with the negative diffractive focus results being on the bottom. The maximum of the fitted curve is given by the dashed line.

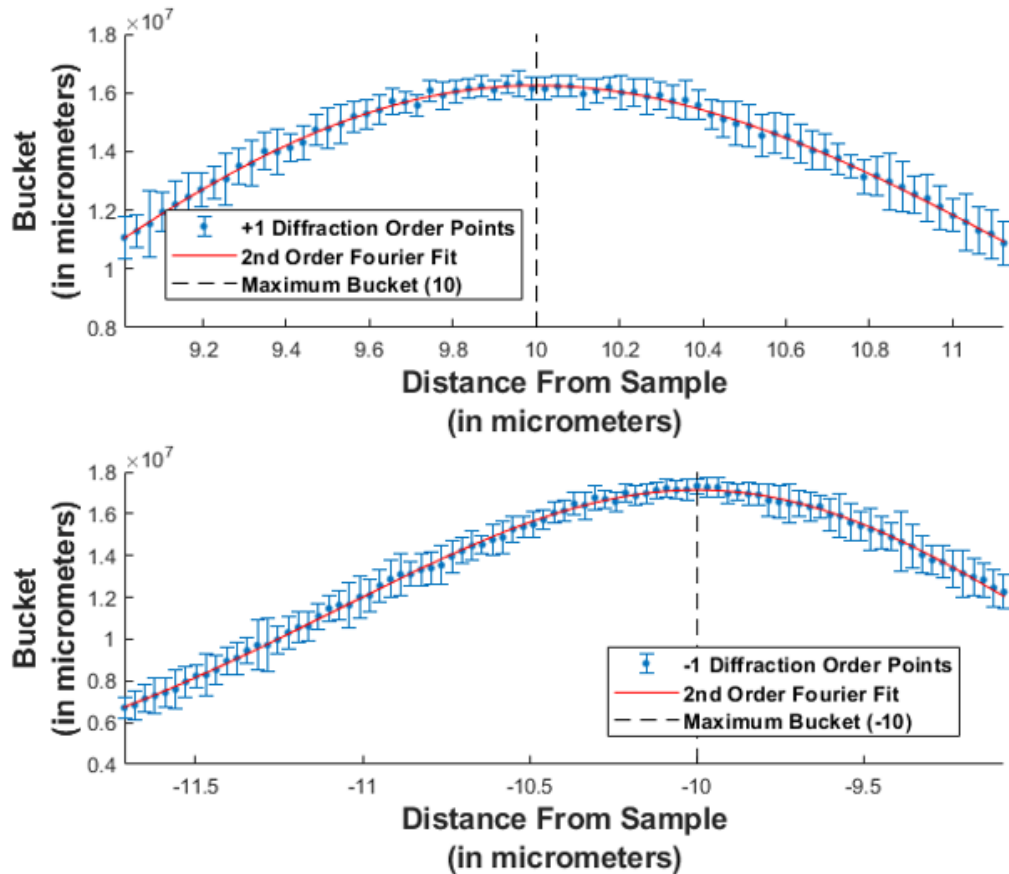


Figure 22. Illustrated is the Power in a Bucket values obtained when scanning near the foci for the sample illuminated with a beam of bandwidth centered at 800nm with a 25nm FWHM. After progressing through a neutral density filter, the power of the beam is 27.16mW, and the intensity at the sample is approximately $0.6761\text{MW}/\text{cm}^2$. Using the methods discussed in the Subsection “Power in a Bucket Method” in Section 2.7, an array of power values are obtained for varying voltage readouts of the z-piezo motor near the focus of the sample. The results near the positive diffractive focus of the metalens are on the top, with the negative diffractive focus results being on the bottom. The maximum of the fitted curve is given by the dashed line.

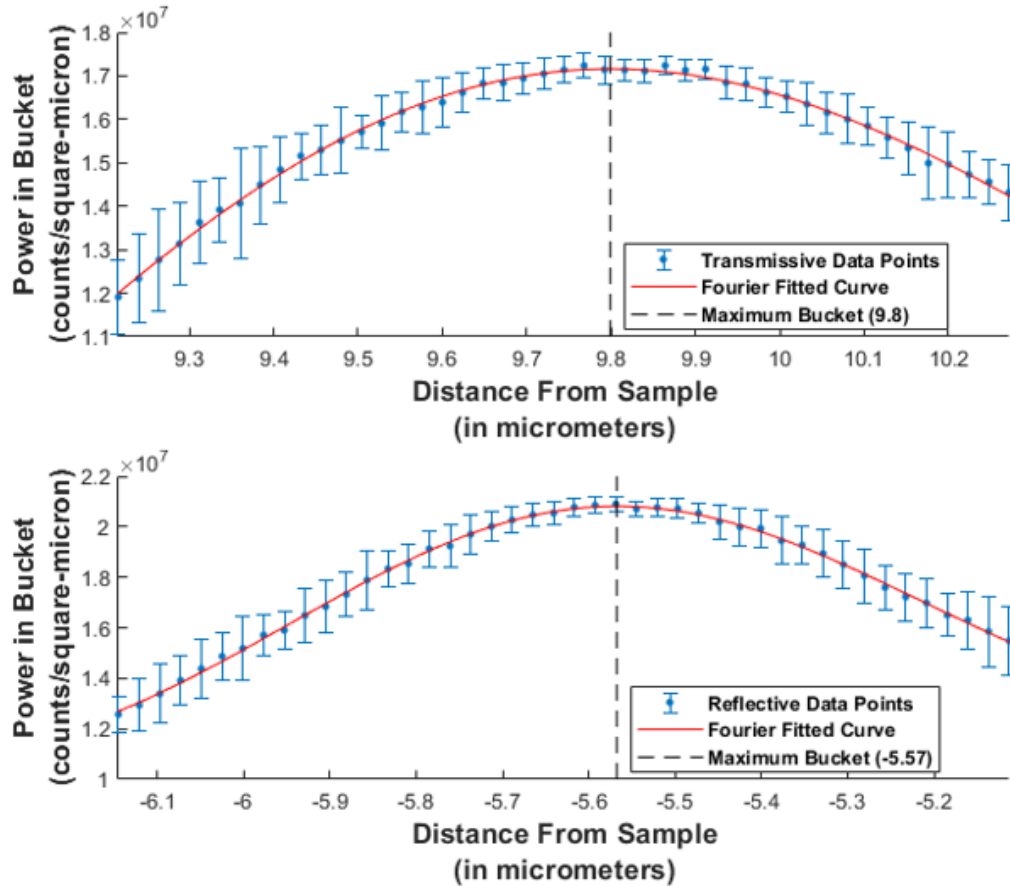


Figure 23. Illustrated is the Power in a Bucket values obtained when scanning near the foci for the sample illuminated with a beam of bandwidth centered at 800nm with a 25nm FWHM. After progressing through a neutral density filter, the power of the beam is 187.1mW, and the intensity at the sample is approximately 4.658MW/cm². Using the methods discussed in the Subsection “Power in a Bucket Method” in Section 2.7, an array of power values are obtained for varying voltage readouts of the z-piezo motor near the focus of the sample. The results near the positive diffractive focus of the metalens are on the top, with the negative diffractive focus results being on the bottom. The maximum of the fitted curve is given by the dashed line.

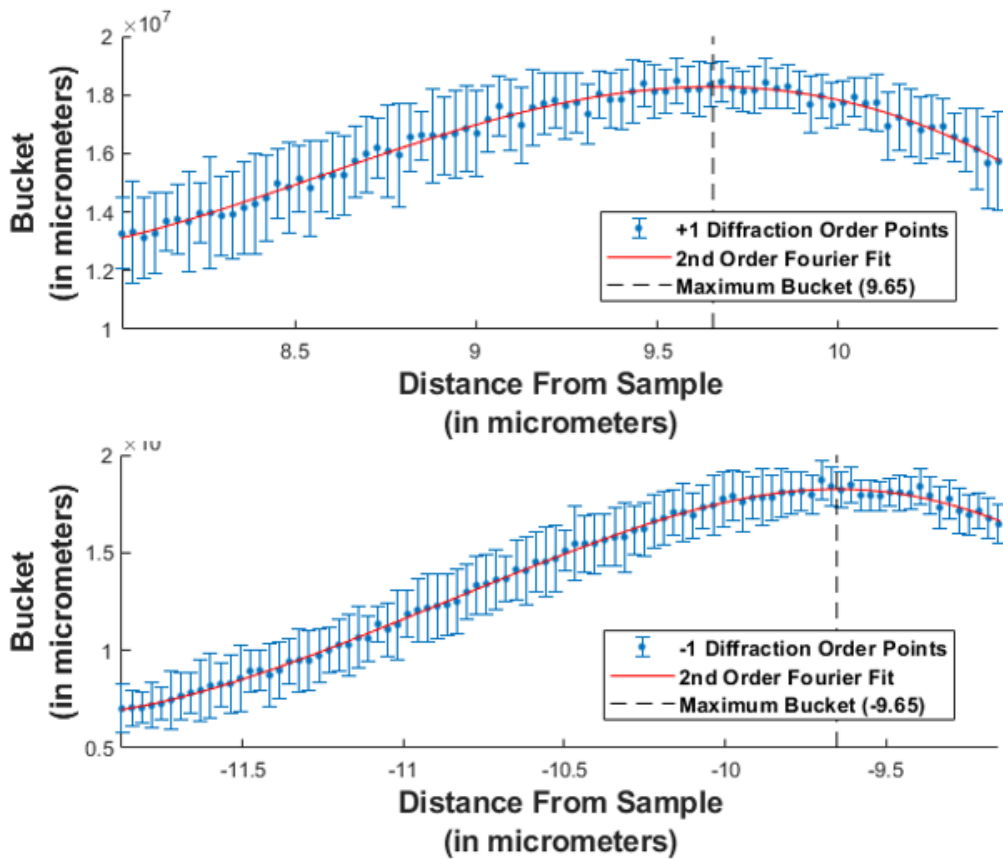


Figure 24. Illustrated is the Power in a Bucket values obtained when scanning near the foci for the sample illuminated with a beam of bandwidth centered at 800nm with a 25nm FWHM. After progressing through a neutral density filter, the power of the beam is 679.8mW, and the intensity at the sample is approximately 16.93MW/cm². Using the methods discussed in the Subsection “Power in a Bucket Method” in Section 2.7, an array of power values are obtained for varying voltage readouts of the z-piezo motor near the focus of the sample. The results near the positive diffractive focus of the metalens are on the top, with the negative diffractive focus results being on the bottom. The maximum of the fitted curve is given by the dashed line.

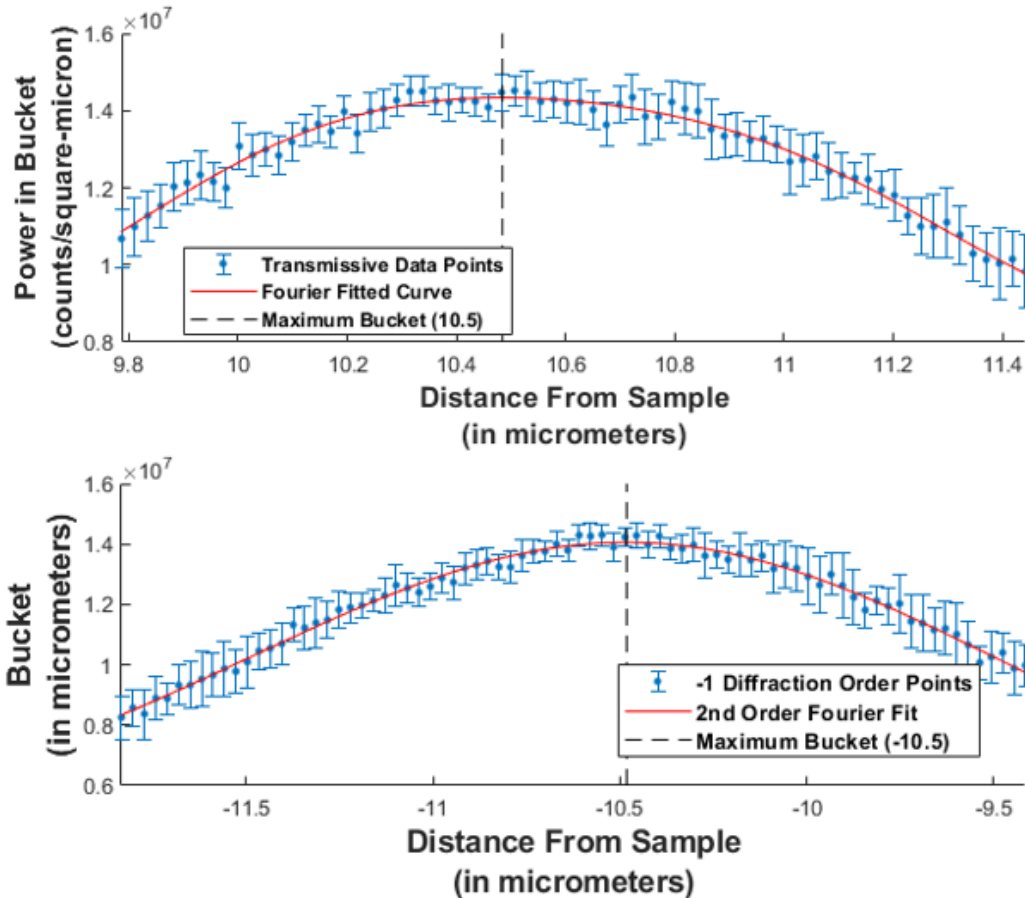


Figure 25. Illustrated is the Power in a Bucket values obtained when scanning near the foci for the sample illuminated with a beam of bandwidth centered at 760nm with a 25nm FWHM. After progressing through a neutral density filter, the power of the beam is 32.863mW, and the intensity at the sample is approximately 0.818MW/cm². Using the methods discussed in the Subsection “Power in a Bucket” in Section 2.7, an array of power values are obtained for varying voltage readouts of the z-piezo motor near the focus of the sample. The results near the positive diffractive focus of the metalens are on the top, with the negative diffractive focus results being on the bottom. The maximum of the fitted curve is given by the dashed line.

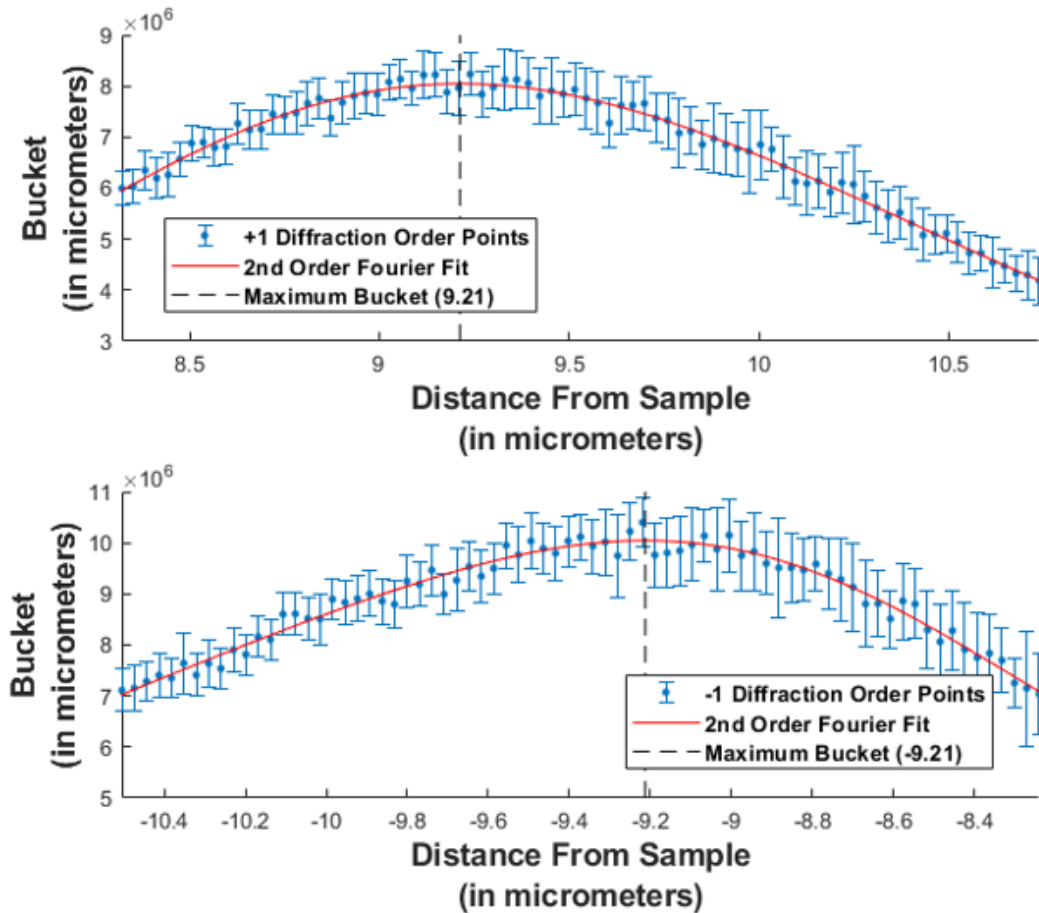


Figure 26. Illustrated is the Power in a Bucket values obtained when scanning near the foci for the sample illuminated with a beam of bandwidth centered at 840nm with a 25nm FWHM. After progressing through a neutral density filter, the power of the beam is 21.67mW, and the intensity at the sample is approximately 0.540MW/cm². Using the methods discussed in the Subsection “Power in a Bucket Method” in Section 2.7, an array of power values are obtained for varying voltage readouts of the z-piezo motor near the focus of the sample. The results near the positive diffractive focus of the metalens are on the top, with the negative diffractive focus results being on the bottom. The maximum of the fitted curve is given by the dashed line.

4.3 Change in Focal Shape Across Scans

This section focuses on analyzing how well the sample metalens focuses reflectively compared to transmissively. The Strehl ratio of the transmissive and reflective focus will be compared across the various intensities and wavelengths, then the R^2 values of the reflective and transmissive focal spots when an Airy Pattern is fit to them will be compared in the same manner, concluding with a comparison of the ‘power in the bucket’ values obtained at the focus for each of the scans.

Strehl Ratio.

In this analysis, the Strehl ratio of the slices at the foci determined using the standard deviation from the $D4\sigma$ method are analyzed. The σ values obtained by in the $D4\sigma$ analysis for the various scans are plugged into (38). The results are listed in Table 9, while Figure 27 illustrates the results comparing the Negative Focus (NF) to the positive focus (PF).

Table 5. NF and PF Strehl Ratios Across Powers and Wavelength Scanned

Wavelength(<i>nm</i>)	Intensity(<i>MW/cm²</i>)	NF Strehl	PF Strehl
800	0.68	0.714	0.773
800	4.66	0.711	0.718
800	16.93	0.706	0.714
760	0.82	0.659	0.687
840	0.54	0.714	0.722

The first takeaway is that the Strehl ratio of these foci are below 0.82, which is not too surprising as this lens does have significant differences from a perfect circular lens. The strehl ratios however are not too far below, all of them being around 0.7. Although these reported strehl ratios are slightly inflated due to limiting the amount of the focus used in calculating the standard deviation to just the width of the central lobe, these values still indicate that this sample, at all intensities measured, has

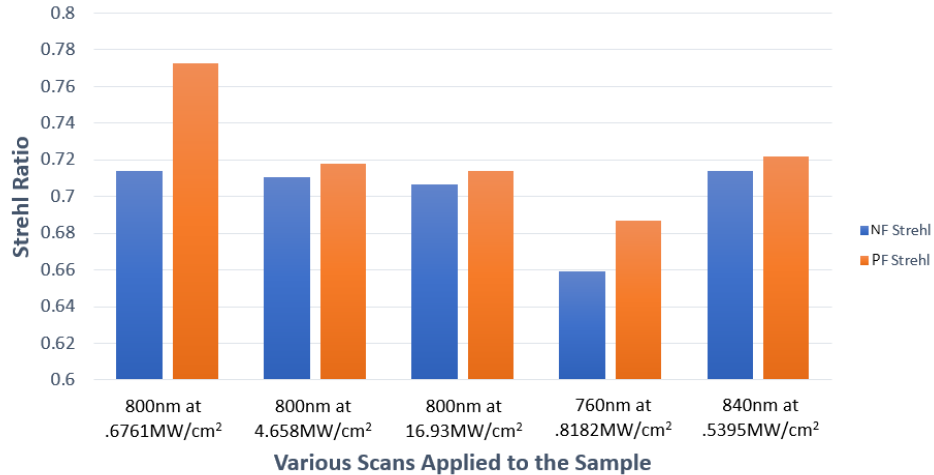


Figure 27. Each red bar represents the Strehl Ratio for the positive diffractive focus, at the beam parameters described below the individual bars. The blue bars, conversely, represent the Strehl Ratio for the negative diffractive foci

a relatively tight focus.

Another important observation is that the foci at the lowest power with the beam centered at 800nm has the highest strehl ratio. This is also expected as the lens was engineered for linear focusing at 800nm. With that said, the other strehl ratios of the other foci are not significantly lower, speaking to effectiveness of the lens at high intensities as well as its broadband capabilities (at least between 760nm and 840nm).

Finally, at all measured intensities and wavelengths, the positive diffractive focus is tighter than the negative diffractive focus. Again this is not surprising as this is the purpose for which the lens was engineered. What is interesting is that in all cases except the low intensity scan at 800nm, and at 760nm, the strehl ratios of the positive diffractive and negative diffractive foci are within 0.008 of each other. Even the 800nm and 760nm scans yield foci within .06 of each other. This shows that the lens, in the range measured, negative diffractively focuses almost as tightly as it does

positively. Given the power is approximately equal in both focii, it would indicate that the lens focuses almost just as well negative diffractively as it does positively.

R^2 Value of fit to Airy.

Whereas the strehl ratio analysis measures the spread of the focus at the various intensities and wavelengths measured, and by nature of the Strehl ratio, the amount of wavefront aberration present compared to the focusing of the ideal circular lens, this analysis compares the focus to that of the shape of the ideal focus. This comparison is more informative as to the shape of the focus.

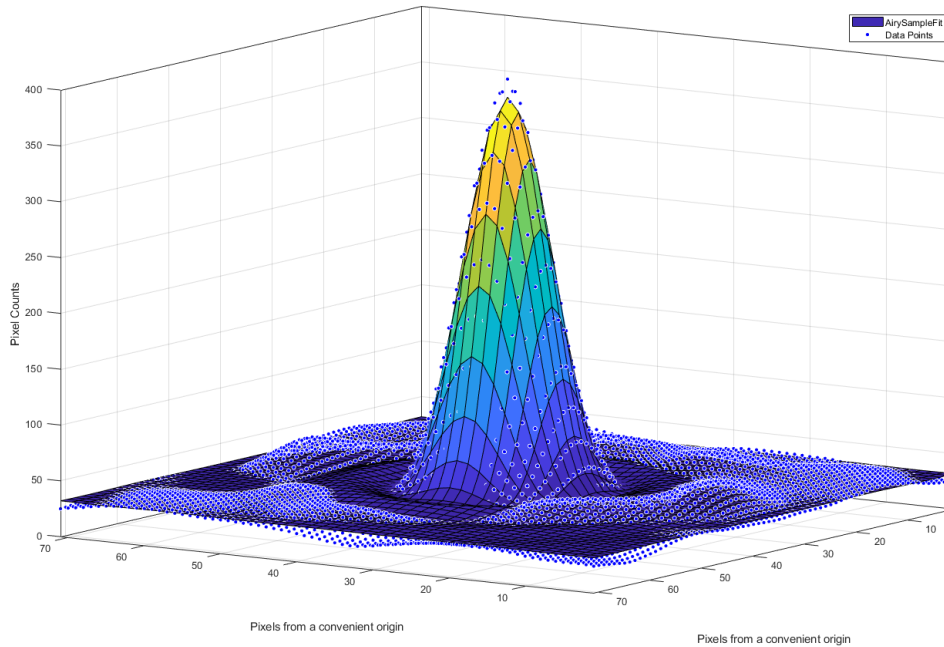


Figure 28. The surface in this 3D plot represents the Airy fit applied to the data points, whereas the dots are the data points. This sample is taken around the positive diffractive focus of the medium power scan ($4.65 MW/cm^2$) with a bandwidth centered at 800 nm. Although it is not a perfect fit, and towards the outer rings it deviates more, it illustrates that the general shape of the focus is similar to an Airy.

After fitting the focal slice for the various wavelengths and intensities to (55), the resulting R^2 values are given in Table 6, and the results are graphed in Figure

29. An example of the fit taken at the transmissive focus at 4.66 MW/cm^2 can also be seen in Figure 28.

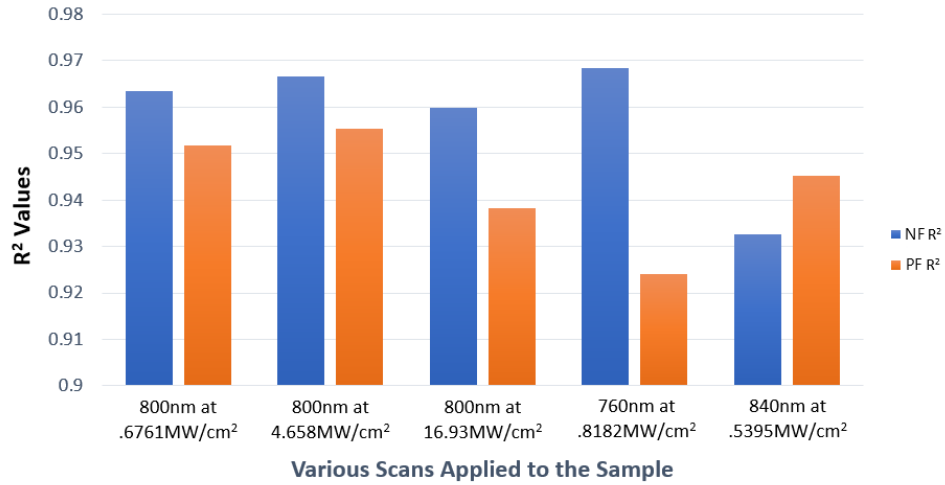


Figure 29. Each red bar represents the R^2 values for the positive diffractive focus when fit to an Airy Pattern, at the beam parameters described below the individual bars. The blue bars, conversely, represent the R^2 for the negative diffractive foci

Table 6. Reporting R^2 values of the scans

Wavelength(nm)	Intensity(MW/cm ²)	RF R^2	TF R^2
800	16.93	0.960	0.938
800	4.66	0.967	0.955
800	0.68	0.963	0.952
760	0.82	0.969	0.924
840	0.54	0.933	0.945

The most obvious trend across the scans is that in almost all cases except the scans taken at 840nm, the reflective focal scan has an R^2 value above its paired transmissive focus. It was expected that, as the lens is designed for transmissive focusing, that the transmissive focus would closer resemble the ideal circular lens. It is possible, as this analysis includes two rings beyond the central lobe, this increased deviation takes place due to the transmissive focus having more power in its higher order rings that do not match up with the airy pattern rings. In order to confirm this, the R^2

analysis could be re-done with just the central lobe and see if this makes a difference, as well as redoing the strehl ratio analysis. If the causes for the lower R^2 value in the transmissive focus comes from the outer rings, then performing the strehl ratio analysis with the same window size would likely show that the transmissive focus has a higher standard deviation, and thus a smaller strehl ratio.

With all of that said, all of the R^2 values are above 0.92, with most around 0.95. This indicates that even including the outer rings, the shape of the focus, resembles an airy pattern, telling us that the focusing is pretty good across all scenarios. With this said, it is entirely possible that another fitting function may match the shape of the focuses analyzed better, but this does is a quantitative measurement confirming the general shape of the focus, and tells that it does not vary significantly across intensities and wavelengths.

Maximum Bucket Values.

The previous two methods of analyzing the focus give analysis of how the lens generally performs. In this method, as the pixel counts are not calibrated to metric units of power, reporting the maximum bucket values is only useful in comparing the values obtained at each positive and negative focal spot relative to each other. The results are given in Table 7. In the Table 7, PiB stands for ‘Power in Bucket’, RF for ‘Reflective Focus’, and TF for ‘Transmissive Focus’.

Table 7. Power in a Bucket at the Focus of Scans

$\lambda(\text{nm})$	Intensity(MW/cm^2)	PiB at RF(counts/ m^2)	PiB at TF(counts/ m^2)
800	16.93	1.82×10^7	1.83×10^7
800	4.66	1.72×10^7	2.08×10^7
800	0.68	1.62×10^7	1.71×10^7
760	0.82	1.43×10^7	1.40×10^7
840	0.54	8.05×10^6	1.00×10^7

As the pixels had different gains along each scan that was done, and all that is being compared is the transmissive and reflective focii in each scan, it is easier to view the results by dividing the pixel counts of each focal point by the pixel counts at the scan's transmissive focal point. This gives the power in the bucket value for the reflective focus as a percentage of the transmissive focus. The results are listed in Table 8 and graphed in Figure 30.

Table 8. Table Comparing Pixel Counts Between Reflective and Transmissive Focus of Each Scan

$\lambda(\text{nm})$	Intensity(MW/cm^2)	% of TF Power at RF
800	16.93	99.9
800	4.66	82.4
800	0.68	94.9
760	0.82	102.1
840	0.54	80.3

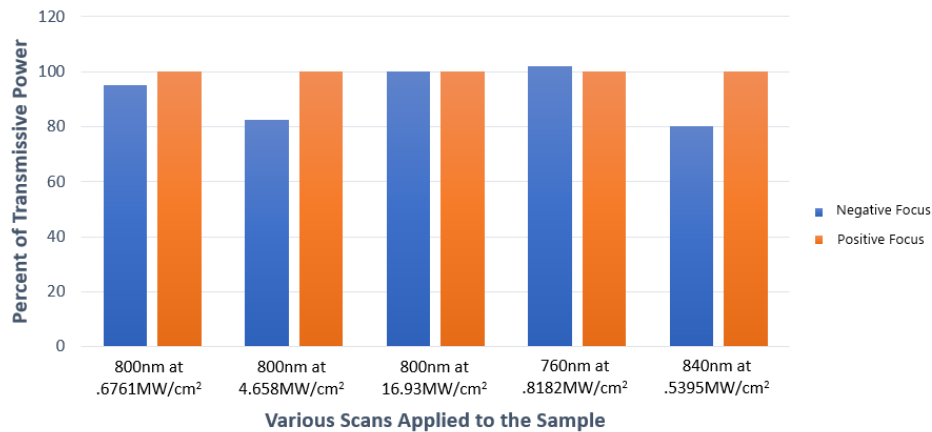


Figure 30. Each red bar represents the percent of positive diffractive focal power is at the positive diffractive focus. All red values then will clearly be 1 then, they are included for better visual comparison to their negative diffractive focus values. The blue bars, conversely, represent the percent of positive diffractive focal power is at the negative diffractive focus

As is expected, in nearly all of the scans, the transmissive focus contains more of the power than the reflective focus. The exception to this is when the sample's

focus is analyzed at a bandwidth centered at 760nm. It is possible that as the sample and the TiN rods were optimized for transmission at 800nm, this occurs simply because at lower wavelengths the sample reflects more. It is interesting though that at $4.658MW/cm^2$ there is more relative power in the transmissive focus than at low powers. In order to accurately characterize this behavior, more scans would need to be done, however this indicates that most power is distributed into the transmissive focus at an intensity between the low intensity scanned and the high intensity.

The power of the reflective focus is on the same order of magnitude as that of the transmissive focus, with the greatest difference only being just under 20 percent. Given the previous methods of focal analysis in which it was determined that the spread and shape were very similar when comparing both focii, now that it is also known that the powers are comparable, it can be said that although the sample does not focus reflectively quite as well as it does transmissively, its reflective performance is very comparable.

4.4 n_2 Analysis From Fourier Lens Model

Both the values obtained using the $D4\sigma$ analysis, and the Power in the Bucket analysis will be used and the respective n values obtained for each will be reported. By utilizing the len's makers formula, setting n_0 to that of TiN, at low intensities,

$$\frac{1}{10 \times 10^{-6}} = (1.7557 - 1)\left(\frac{1}{R} - \frac{1}{R'}\right) \quad (68)$$

giving $\left(\frac{1}{R} - \frac{1}{R'}\right)$ a value of $1.323 \times 10^5 m^{-1}$. This is common for both methods of analysis. From here, beginning with the values from the $D4\sigma$, and by applying (57) to the next highest intensity scanned,

$$\frac{1}{9.728 \times 10^{-6}} = (n_0 + n_2 I - 1)(1.323 \times 10^{-7}) \quad (69)$$

With the intensity being $4.67 \times 10^{12} [W/m^2]$, solving for n_2 yields $-4.563 \times 10^{-15} m^2/W$. With the n_2 value for TiN being $-1.3 \times 10^{-15} [m^2/W]$, this tells that this data point reports an n_2 value slightly greater than three times higher than the value in the material itself. Repeating the same process for the highest intensity yields an n_2 value of -1.629×10^{-15} . Although this value is not as high as that obtained for the medium intensity scan, it is still greater than the nonlinear index of the material itself. In order to completely understand the difference between these numbers, more scans would have to be taken. The only thing that can be said for sure is that at some point the effective index of the lens does not strictly follow Equation (57) most likely due to the saturation of the nonlinear effect, however for all intensities measured, the nonlinear response is still greater than that of the material itself.

The same process can be applied to the results obtained from the "Power in a Bucket" analysis. The results for both methods are summarized in Table 9.

Table 9. Table Summarizing results of Scans

Method	$n_2[\frac{m^2}{W}]$ at $4.658MW/cm^2$	$n_2[\frac{m^2}{W}]$ at $16.93MW/cm^2$
$D4\sigma$	-4.562×10^{-15}	-1.629×10^{-15}
Power in a Bucket	-3.3538×10^{-15}	-1.645×10^{-15}

The values obtained at $4.658MW/cm^2$ vary by a factor of almost 1.5. In order to determine which is a better measurement at that point, and where the source of the difference comes from, more intensities would need to be scanned. The n_2 value obtained in the power in the bucket method is closer to the high intensity value though. Interestingly enough however, the high intensity values report very similar n_2 across both methods.

n_{ml} and n_{mnl} analysis.

This analysis is very similar to the analysis done in the previous section, with the difference being the application of Equation (59) and Equation (60). Using these equations then and the data above, assuming that the sample does not have nonlinear effects at the lowest intensity, $n_{ml} = \frac{1}{10 \times 10^{-6}m}$. This assumption is used for both methods. Using this, the results for both the $D4\sigma$ and the power in the bucket method can be summarized in Table 10.

Table 10. n_{mnl} values for different focal length analysis methods at both high power scans

Method	$n_{mnl}[\frac{m}{W}]$ at $4.66MW/cm^2$	$n_{mnl}[\frac{m}{W}]$ at $16.93MW/cm^2$
$D4\sigma$	-6.04×10^{-10}	-2.16×10^{-10}
Power in a Bucket	-4.44×10^{-10}	-2.18×10^{-10}

4.5 n_2 Analysis From Phase Zone Plate Model

Rather than making the assumption that the index of the lens is equal to that of TiN, treating the lens as a Phase Zone Plate and Rayleigh Sommerfeld propagating the phase profile, the index at low intensity is determined by plugging in various index values for the meta-pillars until the result propagates to a focus at 10 microns. For this reason, the first table shown is simply the values of the total index at various intensities, then by subtracting the lowest intensity index from the others, and dividing by the higher power intensities (which is obtained from simple algebraic manipulation of (48)), the n_2 values can be reported. Beginning with reporting the total effective index,

Table 11. n_{mnl} values for different focal length analysis methods at both high power scans

Method	n at $.69MW/cm^2$	n at $4.66MW/cm^2$	n at $16.93MW/cm^2$
$D4\sigma$	$7.22 \pm .005$	$7.84 \pm .005$	$7.99 \pm .005$
Power in a Bucket	$7.22 \pm .005$	$7.68 \pm .005$	$7.99 \pm .005$

And after applying the manipulation above, $n_2 = (n(I) - n_0)/I$, which gives the effective nonlinear index values of

Table 12. n_{mnl} values for different focal length analysis methods at both high power scans

Method	$n_2[\frac{m^2}{W}]$ at $4.66MW/cm^2$	$n_2[\frac{m^2}{W}]$ at $16.93MW/cm^2$
$D4\sigma$	$1.331 \times 10^{-11} \pm 2 \times 10^{-13}$	$4.548 \times 10^{-12} \pm 6 \times 10^{-14}$
Power in a Bucket	$9.875 \times 10^{-12} \pm 2 \times 10^{-13}$	$4.548 \times 10^{-12} \pm 6 \times 10^{-14}$

Comparing these effective nonlinear index values of the lens to that of TiN (again, $-1.3 \times 10^{-15}[m^2/W]$) give values that are over 3 orders of magnitude greater than that of the bulk material! Given that this method of analysis is more sound than that of the Fresnel Lens model, and that still showed a greater magnitude of nonlinear index,

it suggests that the actual effective nonlinear index of this lens may actually be greater than even these values which are 10^3 greater in magnitude.

V. Conclusions

5.1 Summary

A sample metalens generated by depositing Titanium Nitride onto Aluminum Oxide designed to focus at 10 microns was tested at three intensities with a bandwidth centered at a wavelength of 800nm, as well as at low intensities with the bandwidth centered at 840nm, and again at 760nm. Two different methods were used in determining where the focus was located, the power in the bucket method, and the $D4\sigma$ method. At high intensities and at low intensities, both methods approximately agreed as to the location of the focal spot. At the intensity between the high and low intensities, these two methods were significantly different. Further focal analysis was done using the frames obtained using the $D4\sigma$ method, at which point it was determined that in almost all cases, the reflective focus of the metalens had a higher spread and lower power than the transmissive focus, but only very slightly. This indicates that it is likely that rather than the lens transmitting most of the incident power, that it probably reflects about half of it, as expected for a plasmonic lens with $\mu_m \approx 1$.

Regarding which method should be used to determine where the focus of the lens is, the power in the bucket method makes more sense. As the focusing behavior of the metalens is not the same as that of a typical refractive lens, it is possible that some of this unaccounted for behavior skewed the σ values to report smaller values where there is the most power in the center of the lobe, and larger values elsewhere. The benefit of the power in the bucket method is that for applications, maximum power incident on a detector or in an area is what is desired. If using the $D4\sigma$ method for determining the focal length, it was shown that the detector might be able to read a higher value at some location away from the reported $D4\sigma$ focal length. Although

neither method assumes the shape of the focus (they are shape agnostic), to a degree, the $D4\sigma$ method assumes the focusing behavior when used to determine where the focus is.

With that said, the lens, at all data points taken showed nonlinear responses indicative of non-linear properties of the lens greater than those of TiN or Al_2O_3 . The values obtained did not indicate a linear relationship between the nonlinear index and intensity as was expected, so more measurements will need to be taken to determine the source of this. In the end, the goal of showing an increased nonlinear response from the lens relative to the material was achieved, and for the Fresnel Zone Plate model, orders of magnitude increased.

5.2 Benefits and Limitations

The primary benefit of this analysis is that it reported nonlinear focusing due to the geometry of the TiN deposits to form a metalens. This is promising for potential high energy applications, such as the aforementioned optical computing. Various wavelengths were used as well, and at bandwidths centered 40 nm from the bandwidth center for which the the lenses were designed, they performed comparable to the lens performance at center wavelength. This speaks to the broadband capabilities of the lens.

The primary limitation in this analysis is that, with only three intensity measurements, and only three wavelengths measured, the only real takeaway is that the power in the bucket method and the $D4\sigma$ methods yield slightly different results for where the focus should be reported, and that there is certain nonlinear focusing.

5.3 Recommendations for Future Work

As only three intensities were used to determine the nonlinear index of refraction, and only three wavelengths were used to determine the lens' broadband performance, the next step would be to do a more complete intensity sweep and fill in the gaps. This extra knowledge should give a more complete picture of the behavior and nonlinear focusing properties of the lens. More measurements at varying bucket sizes, and increased area included in the $D4\sigma$ analysis could also be informative as to how the lens focuses at higher intensities. When doing a power in the bucket analysis as well, calibrating the pixel counts to metric units would be informative with regards to the lens performance. This analysis showed that across a few wavelengths and across an intensity spectrum, the focii are a certain shape and the reflective and transmissive focii are not all that different, but it says nothing to the lens efficiency (power in the focus/incident power).

As the voltage values input into the z-piezo needed to be adjusted by hand, another step to simplifying the process of analyzing these meta lenses would be to develop a method to autonomously scan and sweep the planes near the focal length of these lenses. Furthermore, as these metalenses have been proven to have high broadband performance, analyzing these lenses with a wider range of wavelengths could prove to be an important analysis as well.

Finally, although relative to the focal length of the micro lenses, the beam was fairly collimated, doing an analysis of how these lenses focus light that is not collimated has the potential to yield interesting results, especially at varying intensities and wavelengths. Depending on the lens performance in this situation, it could increase the potential applications as it would show that the incoming beam does not need to be collimated.

Appendices

NONLINEAR CHARACTERIZING OF A NEW TITANIUM NITRIDE ON
ALUMINUM OXIDE METALENS

A. Small Errors in Focal Length

When analyzing the uncertainty in the focal length, the reported values were much smaller than they realistically should be, and an order of magnitude smaller than the equipment was capable of measuring in some cases. When simply applying a Fourier fit, with a horizontal offset (ideally to determine where the minimum is and uncertainty in the minimum), the uncertainty was very large, independent of model, as small changes in the other variables, greatly affected the horizontal offset.

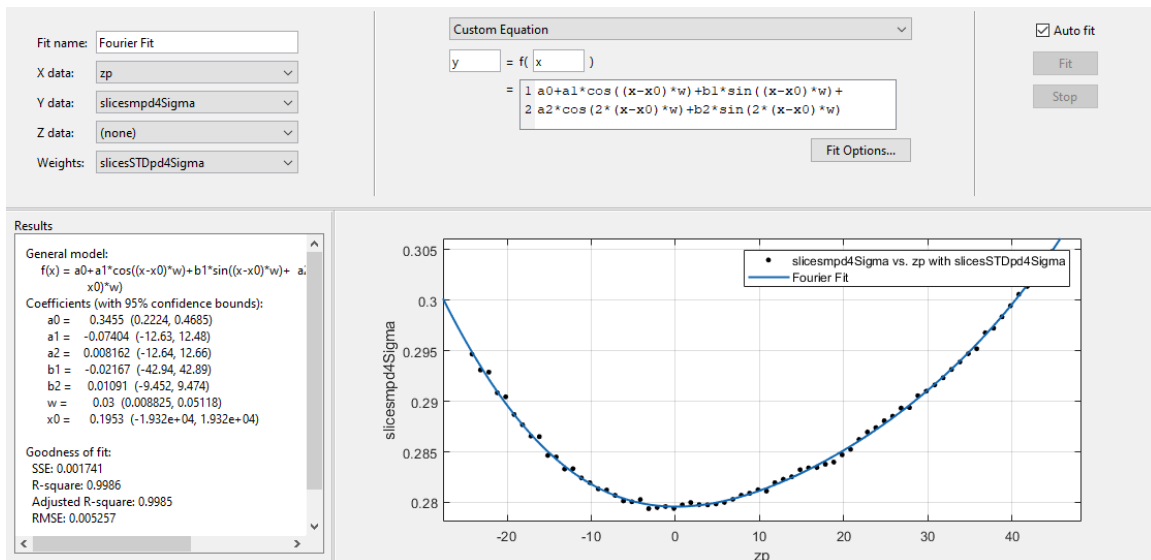


Figure 31. A second order Fourier Curve is fit to the data points, with an x_0 offset. There is a very large uncertainty in the x_0 , but the other values have relatively low uncertainties.

Moving to get more realistic uncertainties in the fit, rather than defining an equation to fit to, the built in second order Fourier fit was used, and obtained a very

reasonable fit, as shown.

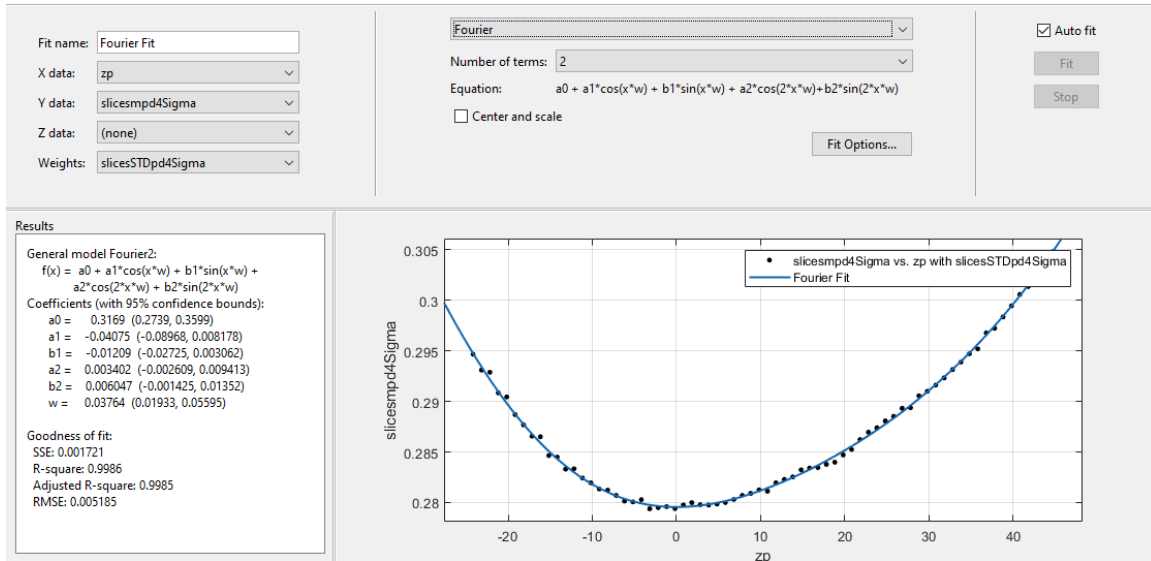


Figure 32. Without any x_0 , Matlab provides its automated second order Fourier fit and the outputs for the individual variables can be seen, all with reasonable uncertainty.

From here, these number were used, and plugged back into the equation from 31. This meant that the shape of the curve was fixed, so uncertainty in the other variables didn't blow the x_0 out of proportion. The uncertainty in the fit arose from the standard deviation in each of the data points (shown as error bars in the plots included in the body of the thesis).

Due to the fact that the left and right uncertainty in the focus comes from the horizontal uncertainty of a curve that's shape is predefined to fit the data, the uncertainty reported is smaller than it realistically should be. This is the nature of the way the data was obtained and analysis methods available.

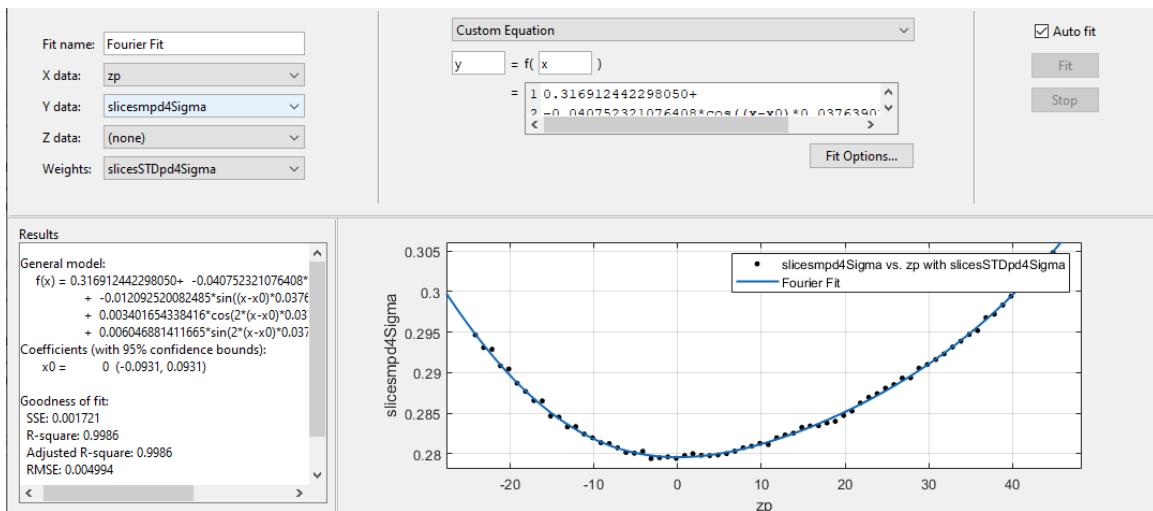


Figure 33. Similar to the base Fourier fit with "x₀" included, however the results from Matlabs' Fourier fit are plugged into the variables, leaving only the x₀ to be solved for.

Bibliography

1. D. Kajfez and P. Guillon, *Dielectric Resonators*. Artech House microwave library, Artech House, 1986.
2. J. Hu, “Evolutionary design and prototyping of single crystalline titanium nitride lattice optics,” *ACS Photonics*, pp. 606–612, 2017.
3. N. Kinsey, “Effective third-order nonlinearities in metallic refractory titanium nitride thin films,” *Optical Society of America*, vol. 5, no. 11, pp. 201–208, 2015.
4. N. Kinsey, A. A. Syed, D. Courtwright, C. DeVault, C. E. Bonner, V. I. Gavrilenko, V. M. Shalaev, D. J. Hagan, E. W. V. Stryland, and A. Boltasseva, “Effective third-order nonlinearities in metallic refractory titanium nitride thin films,” *Opt. Mater. Express*, vol. 5, pp. 2395–2403, Nov 2015.
5. M. Born and E. Wolf, *Principles of Optics: Electromagnetic Theory of Propagation, Interference and Diffraction of Light (7th Edition)*. Cambridge University Press, 7th ed., 1999.
6. M. Fox, *Optical Properties of Solids*. Oxford Master Series in Physics, OUP Oxford, 2010.
7. A. Lahiri, “Chapter 2 - foundations of ray optics,” in *Basic Optics* (A. Lahiri, ed.), pp. 141 – 202, Amsterdam: Elsevier, 2016.
8. N. Yu, P. Genevet, M. A. Kats, F. Aieta, J.-P. Tetienne, F. Capasso, and Z. Gaburro, “Light propagation with phase discontinuities: Generalized laws of reflection and refraction,” *Science*, vol. 334, no. 6054, pp. 333–337, 2011.
9. R. J. Bell, K. R. Armstrong, C. S. Nichols, and R. W. Bradley, “Generalized laws of refraction and reflection*,” *J. Opt. Soc. Am.*, vol. 59, pp. 187–189, Feb 1969.
10. X. Luo, M. Pu, X. Ma, X. Li, and W. Zhu, “Taming the electromagnetic boundaries via metasurfaces : From theory and fabrication to functional devices,” 2015.
11. “Geometric optics.” Harvard Lecture, 2007.
12. E. Bayati, A. Zhan, S. Colburn, M. V. Zhelyeznyakov, and A. Majumdar, “Role of refractive index in metalens performance,” *Appl. Opt.*, vol. 58, pp. 1460–1466, Feb 2019.
13. H.-T. Chen, A. J. Taylor, and N. Yu, “A review of metasurfaces: physics and applications,” *Reports on Progress in Physics*, vol. 79, p. 076401, jun 2016.
14. T. Zentgraf, “Imaging the rainbow,” *Nature Nanotechnology*, vol. 13, 01 2018.

15. S. Lal, S. LINK, and N. Halas, *Nano-optics from sensing to waveguiding*, pp. 213–220. 08 2009.
16. F. Aieta, P. Genevet, M. Kats, and F. Capasso, “Aberrations of flat lenses and aplanatic metasurfaces,” *Optics express*, vol. 21, pp. 31530–9, 12 2013.
17. S. Maitra, “3 - nanoceramic matrix composites: types, processing and applications,” in *Advances in Ceramic Matrix Composites* (I. Low, ed.), pp. 27 – 42, Woodhead Publishing, 2014.
18. O. Sakai, A. Iwai, and Y. Omura, “Invariance of parameter identification in multiscales of meta-atoms in metamaterials,” *Advances in Physics: X*, vol. 3, no. 1, p. 1433551, 2018.
19. M. N. Polyanskiy, “Refractive index database.” <https://refractiveindex.info>. Accessed on 2019-04-22.
20. P. Patsalas, N. Kalfagiannis, and S. Kassavetis, “Optical properties and plasmonic performance of titanium nitride,” *Materials*, vol. 8, no. 6, pp. 3128–3154, 2015.
21. P. Auerkari, *Mechanical and physical properties of engineering alumina ceramics*. Technical Research Centre of Finland Espoo, 1996.
22. S. Wang, J. Zhang, D. Luo, F. Gu, D. Tang, Z. Dong, G. Tan, W. Que, T. Zhang, S. Li, and L. Kong, “Transparent ceramics: Processing, materials and applications,” *Progress in Solid State Chemistry*, vol. 41, no. 1, pp. 20 – 54, 2013.
23. T. Sundari, R. Ramaseshan, F. Jose, S. Dash, and A. K. Tyagi, “Temperature dependence of dielectric constants in titanium nitride,” *J. Appl. Phys.*, vol. 115, 08 2013.
24. W. b. AZoM, “Gold - physical, mechanical, thermal and electrical properties of gold - world gold council,” Aug 2018.
25. M. Baucchio, *ASM engineered materials reference book*. Materials Park, OH : ASM International, 2nd ed ed., 1994. Cover title: ASM engineered materials reference book.
26. M. R. Vissers, J. Gao, D. S. Wisbey, D. A. Hite, C. C. Tsuei, A. D. Corcoles, M. Steffen, and D. P. Pappas, “Low loss superconducting titanium nitride coplanar waveguide resonators,” *Applied Physics Letters*, vol. 97, no. 23, p. 232509, 2010.
27. D. Wisbey, J. Gao, M. Vissers, J. Kline, M. Weides, and D. Pappas, “Design and fabrication of high q titanium nitride resonators,” 03 2011.
28. F. Wang and Y. R. Shen, “General properties of local plasmons in metal nanostructures,” *Phys. Rev. Lett.*, vol. 97, p. 206806, Nov 2006.

29. V. Giannini, A. I. Fernández-Domínguez, S. C. Heck, and S. A. Maier, “Plasmonic nanoantennas: Fundamentals and their use in controlling the radiative properties of nanoemitters,” *Chemical Reviews*, vol. 111, no. 6, pp. 3888–3912, 2011. PMID: 21434605.
30. F. E. Grubbs, “On the distribution of the radial standard deviation,” *The Annals of Mathematical Statistics*, vol. 15, no. 1, pp. 75–81, 1944.
31. A. E. Siegman, “How to (maybe) measure laser beam quality,” in *DPSS (Diode Pumped Solid State) Lasers: Applications and Issues*, p. MQ1, Optical Society of America, 1998.
32. S. Kaim, S. Mokhov, R. Drachenberg, L. Glebov, and B. Zeldovich, “Characterization of beam quality by the “power-in-the-bucket”,” 10 2011.
33. E. Hecht, *Optics*. Pearson, 2016.
34. A. van den Bos, “Aberration and the strehl ratio,” *J. Opt. Soc. Am. A*, vol. 17, pp. 356–358, Feb 2000.
35. E. Bayati, “The role of refractive index in metalens performance,” Master’s thesis, University of Washington Seattle, 2017.
36. B. E. A. Saleh and M. C. Teich, *Fundamentals of photonics; 2nd ed.* Wiley series in pure and applied optics, New York, NY: Wiley, 2007.

REPORT DOCUMENTATION PAGE

Form Approved
OMB No. 0704-0188

The public reporting burden for this collection of information is estimated to average 1 hour per response, including the time for reviewing instructions, searching existing data sources, gathering and maintaining the data needed, and completing and reviewing the collection of information. Send comments regarding this burden estimate or any other aspect of this collection of information, including suggestions for reducing this burden to Department of Defense, Washington Headquarters Services, Directorate for Information Operations and Reports (0704-0188), 1215 Jefferson Davis Highway, Suite 1204, Arlington, VA 22202-4302. Respondents should be aware that notwithstanding any other provision of law, no person shall be subject to any penalty for failing to comply with a collection of information if it does not display a currently valid OMB control number. **PLEASE DO NOT RETURN YOUR FORM TO THE ABOVE ADDRESS.**

1. REPORT DATE (DD-MM-YYYY) 08-29-2019		2. REPORT TYPE Master's Thesis		3. DATES COVERED (From — To) Aug 2017 — August 2019	
4. TITLE AND SUBTITLE NONLINEAR CHARACTERIZING OF A NEW TITANIUM NITRIDE ON ALUMINUM OXIDE METALENS				5a. CONTRACT NUMBER	
				5b. GRANT NUMBER	
				5c. PROGRAM ELEMENT NUMBER	
6. AUTHOR(S) Michael A. Cumming				5d. PROJECT NUMBER	
				5e. TASK NUMBER	
				5f. WORK UNIT NUMBER	
7. PERFORMING ORGANIZATION NAME(S) AND ADDRESS(ES) Air Force Institute of Technology Graduate School of Engineering and Management (AFIT/ENP) 2950 Hobson Way WPAFB OH 45433-7765				8. PERFORMING ORGANIZATION REPORT NUMBER AFIT/GAP/ENP/19-D/012	
9. SPONSORING / MONITORING AGENCY NAME(S) AND ADDRESS(ES) Department of Engineering Physics 2950 Hobson Way WPAFB OH 45433-7765 DSN 271-0690, COMM 937-255-3636 Email: michael.cumming@afit.edu				10. SPONSOR/MONITOR'S ACRONYM(S) AFWA	
				11. SPONSOR/MONITOR'S REPORT NUMBER(S)	
12. DISTRIBUTION / AVAILABILITY STATEMENT DISTRIBUTION STATEMENT A: APPROVED FOR PUBLIC RELEASE; DISTRIBUTION UNLIMITED.					
13. SUPPLEMENTARY NOTES					
14. ABSTRACT A sample metalens generated from Titanium Nitride deposited onto Aluminum Oxide was designed to focus at 10 microns with a beam centered at 800nm, and when analyzed with high intensity illumination was found to have a focal length of $9.65 \mu\text{m}$ at an intensity of $16.93 [MW/cm^2]$. The change observed shows that for this lens, the effective nonlinear index of refraction is certainly greater than the nonlinear index of just the lens itself, at $-1.6239 \times 10^{-15} [m^2/W]$ compared to the materials $-1.3 \times 10^{-15} [m^2/W]$. The focus of the metalens was analyzed, both reflectively and trasmissively, and although there was nonlinear tightening due to the high intensity, the power in the reflective focus is about the same as the power in the transmissive focus, cutting the efficiency in two. Finally a method of reporting the nonlinear focusing properties of the metalenses that combines the index of a lens and the radii of a lens from the len's makers equation into one is proposed to better understand the focusing behavior of the lenses at higher intensities.					
15. SUBJECT TERMS Metalens, Metasurface, n_2 , Nonlinear, Titanium Nitride, Aluminum Oxide					
16. SECURITY CLASSIFICATION OF:			17. LIMITATION OF ABSTRACT	18. NUMBER OF PAGES	19a. NAME OF RESPONSIBLE PERSON
a. REPORT	b. ABSTRACT	c. THIS PAGE			Dr . M. Ferdinandus
U	U	U	U	79	19b. TELEPHONE NUMBER (include area code) (781) 541-0071; mrf@knights.ucf.edu